
Study of Microstructure Emission in Radio Pulsars using GMRT data

*A thesis Submitted
in Partial Fulfilment of the Requirements
for the Degree of
MASTER OF SCIENCE*

by
Satyam Chandra Mishra

Supervisors:

Prof. Yashwant Gupta¹

Dr. Tuhin Ghosh²

¹National Centre for Radio Astrophysics (NCRA-TIFR), Pune

²National Institute of Science Education and Research, Bhubaneswar



Acknowledgement

I acknowledge with gratitude my indebtedness to my teachers, colleagues, family and friends for their support and motivation throughout my journey in the field of science. To begin with, I would like to thank my supervisor, Prof. Yashwant Gupta for giving me the opportunity to work with him and patiently guiding me throughout this project. I am also grateful to Dr. Tuhin Ghosh, who agreed to my guide from NISER side. I would like to thank the staff members at the National Centre for Radio Astrophysics (NCRA) and the Giant Metrewave Radio Telescope (GMRT) for helping me at various stages of this work. The GMRT is run by the National Centre for Radio Astrophysics of the Tata Institute of Fundamental Research.

Throughout my endeavors, struggles and achievements, my friends and family have always been beside me. I would like to take this opportunity to thank them for everything they have done for me and for standing by me even in the worst of times. They have made me what I am.

Contents

1	Introduction	7
1.1	Background	7
1.2	Motivation	8
1.3	Report Outline	9
2	Pulsar Emission and Effects of the Interstellar Medium	10
2.1	Effects of Interstellar Medium	11
2.1.1	Dispersion	12
2.2	What is Microstructure?	13
2.3	Microstructure Emission Mechanism	14
3	Signal Processing and Observation Details	16
3.1	Signal Processing for Pulsars Observation	17
3.1.1	Incoherent Dedisperion	18
3.1.2	Coherent Dedisperion	18
3.2	Observation Details	20
3.3	Candidate Selection	21
3.4	Microstructure Properties at Dual Frequency	21
3.4.1	Folded profiles and Individual pulses of B2016+28 and B0950+08 . .	22
4	Data Analysis and Algorithms	25
4.1	Autocorrelation Analysis	25
4.1.1	When does the Autocorrelation Function (ACF) fail?	27
4.2	Smoothed Subtraction: Extracting only microstructure feature from the sub-pulse	27

4.3	Microstructure Detection	29
4.4	Analysis Configuration and Changes	30
4.5	Microstructure Widths	30
4.6	Microstructure Periodicity	31
4.7	Cross Correlation Analysis	32
4.7.1	CCF on the residuals	33
4.7.2	Interpolating the CCF peak	34
4.7.3	Dependence of CCF on the phase window	35
5	Micropulse Statistics and Results	37
5.1	Width Distribution	37
5.2	Period Distribution	37
5.3	FFT averaging	42
5.4	Frequency evolution of microstructures	44
5.4.1	CCF distribution in B2016+28 pulsar	44
5.4.2	CCF distribution in B0950+08 pulsar	49
6	Discussion and Conclusion	55
6.1	Discussion	55
6.1.1	Width distribution	55
6.1.2	Periodicity distribution	56
6.1.3	Frequency evolution of the microstructures and dependence on the phase range	56
6.2	Conclusion	57
6.3	Future work	58
A	Does smoothening by Savitzky-Golay preserve the microstructures' properties	59

List of Figures

2-1	Model for the rotating neutron star and its magnetosphere such that the Rotational axis is misalinged with Magnetic axis(refered from Handbook of Pulsars Astronomy.)	10
2-2	An example pulsar with rotation period of 1 second is taken. The pulsar gets stronger with each fold, while the noise strength decreases. (refered from Handbook of Pulsars Astronomy.)	11
2-3	A typical single pulse microstructure emission of B2016+28 (referred from Cordes 1990)	14
2-4	Models for Microstructure Origin	15
3-1	Schematic diagram of Radio Telescope Receiver system (refered from Handbook of Pulsar Astronomy)	17
3-2	Incoherently and coherently dedispersed normalized folded profiles of the pulsar B1937+21 observed with the GMRT at 325 MHz. The pulsar has a period of 1.55 ms and a DM of 71 pc/cc. (Source: Kishalay De and Yashwant Gupta, 2015)	20
3-3	Folded profiles	22
3-4	A single pulse of B2016+28 showing the emission of microstructure riding on a smooth pulse between the phase of 0.31 to 0.34	23
3-5	A single pulse of B0950+08 showing the emission of microstructure riding on a smooth pulse between the phase of 0.74 to 0.82	23

4-1	Schematic of Autocorrelation Function (ACF) of a pulse is shown. Here Δt_μ is micropulse break point and Δt_s is half-width at half-maximum. The narrow spike of width Δt is due to noise in the signal. (refered from article on Pulsars Microstructure by J. M. Cordes 1979)	26
4-2	ACF of the pulse from B0950+08 shown in the figure 3-5	27
4-3	Top plot is showing a single pulse of B0950+08 at 325MHz(Red) and 610MHz(Green). Middle plot is the smoothed pulse. Bottom plot is showing the residual Micropulse obtained after subtraction of smoothed pulse from single pulse. The bottom figure shows the ACF of the residuals.	28
4-4	The CCF plot for the pulse shown in fig 3-5. Time-lag from the graph = 0 bin (Here, 1 time-bin=0.04608ms)	34
4-5	The polynomial fitted CCF plot for the fig 4-4. We note that the reported value of -0.4335 bins is in a good agreement with the manual inspected value of -0.4392 bins	35
4-6	CCF plots for a pulse with different phase windows	35
5-1	For pulsar B0329+54	38
5-2	For pulsar B0950+08	38
5-3	For pulsar B1642-03	39
5-4	For pulsar B2016+28	39
5-5	For pulsar B0329+54	40
5-6	For pulsar B0950+08	40
5-7	For pulsar B1642-03	41
5-8	For pulsar B2016+28	41
5-9	Folded FFT (in orange) compared with the histogram of the detected frequency. Left column is of the 310MHz, and the right one is of the 625MHz observation. Please note: that the frequency is shown in x-axis of the following graphs	43
5-10	The folded profile of B2016+28 with the full range of chosen phase marked with green-dotted lines.	44
5-11	The folded profile of B0950+08 with the full range of chosen phase marked with green-dotted lines.	49

Chapter 1

Introduction

A pulsar is a neutron star - the ultra-dense core that remains after a massive star undergoes a supernova explosion – spinning at very rapid rates ranging from once in a few seconds to as much as ~ 1000 times per second. Since their discovery almost 50 years ago (Hewish et al., 1968), pulsars have revolutionised our understanding of physical processes in the high energy universe. Radio pulsars, in particular, have been studied extensively for a wide range of interesting scientific goals, starting from pulsar timing to understanding the nature of pulsar radio emission. The emission mechanism produces radio frequency radiation that comes out in two beams, one from each pole of the magnetosphere. These rotating beams of radiation are seen by us whenever they intersect our line of sight to the pulsar, much like a lighthouse on the sea-shore. Each rotation of the pulsar thus produces a narrow pulse of radiation that can be picked up by a radio telescope.

1.1 Background

While significant progress has been made in understanding some radio emission characteristics of pulsars, there are still many aspects which remain unexplained by theoretical models. This is in particular, true for various properties of single pulses, since a large fraction of current emission models concentrate on properties of average profiles. It is well known that, at the single pulse level, pulsars show emission on a diverse range of timescales – from subpulses that are typically few milliseconds wide to micropulses that can have timescales of a few microseconds (e.g. Lange et al., 1998) down to intensity oscillations at timescales of a few nanoseconds (see Hankins, 2003).

Microstructure emission has been observed in high time resolution studies of many pulsars, which are characterised by a typical width or time scale of the micropulses, and often show quasi-periodicity, wherein one observes a sequence of repeating micropulses appear one after the other (e.g. Boriakoff, 1981). The broadband nature of the phenomenon indicates that these features are closely related to the magnetospheric radio emission process (Rickett et al., 1975). Several attempts have been made to explain the origin of microstructure emission, and consist of different mechanisms, such as emission by plasma bunches and plasma instabilities. The typical time scale of the micropulses, its bandwidth, and the frequency evolution of the location and width of the micropulses are some of the crucial observational parameters that can help distinguish between the various possible models.

1.2 Motivation

Microstructures are intensity modulation in the bright single pulses. Even though it is a well-known phenomenon, and was discovered very soon after the first observations of pulsars, there are not too many extensive studies of it. The problem arises because of difficulty in conducting a very high time resolution observations which, at low frequencies, need to overcome broadening effects, such as due to dispersion and scattering. Furthermore, not much is known about the detailed micropulse emission properties of millisecond pulsars; primarily due to the intrinsically lower fluxes of these objects compared to normal pulsars, as well as the significantly higher time resolutions required to study them. Microstructures hold a lot of information about the pulsar magnetosphere and are supposed to be occurring due to meter level fluctuation in the magnetosphere atmosphere. Hence its characteristics can help us to find restriction on the pulsar emission process. Investigation of microstructure in these objects have a lot of potential, owing to their significantly different evolutionary histories, and drastically different physical parameters (e.g. period, surface magnetic field) compared to normal pulsars.

In order to obtain sufficient Signal to Noise Ratios (SNRs) at these time resolutions, one requires a very sensitive telescope and/or exceptionally bright pulsars. Hence, most of the significant observations of pulsar microstructure have been carried out by the Arecibo tele-

scope, benefiting from its high sensitivity, but constrained to a specific set of pulsars due to its limited sky coverage. Some other studies have been carried out with the Effelsberg telescope (Lange et al., 1998), while some low frequency studies have been carried out with Russian low frequency instruments (e.g. Kardashev et al., 1978).

Given the steep spectra of these sources, low frequency studies are favoured, but limited due to several factors. One needs to a) have a radio telescope with enough sensitivity to detect single pulses and b) be able to correct for the dispersive effects of the interstellar medium with coherent dedispersion over reasonably large bandwidths. The GMRT provides a unique opportunity to attempt such studies, for a set of carefully selected pulsars that are strong and have dispersion measures not too large to be affected by scattering.

1.3 Report Outline

In this thesis, we present the methodology, data analysis techniques and preliminary the study of microstructure emission, at two different frequencies, using the GMRT. In Chapter 2 we explain the emission properties of typical pulsar, microstructure, proposed mechanism behind microstructure emission and effects caused by ISM to pulsars signal during its travel. Obervation details and radio pulsar observation instrumentation is highlighted in Chapter 3 with some of the typical micropulse examples. Chapter 4 deals with the data analysis process and the algorithms used for micropulse extraction from single pulse and its quantification. Chapter 5 presents the results and corresponding interpretation of the same.

Chapter 2

Pulsar Emission and Effects of the Interstellar Medium

Pulsars are rotating neutron stars, emitting radiation along magnetic axis in a conical form. When rotational axis and magnetic axis are misaligned, we get pulsed emission from them. These pulses are the only source of information and their timing are studied to understand more about them. When we stack these periodic signals and add them, we get a **Folded or Average profile** of that pulsar. The average profile and rotation period are the important characteristics of every pulsar which remain stable for many years.

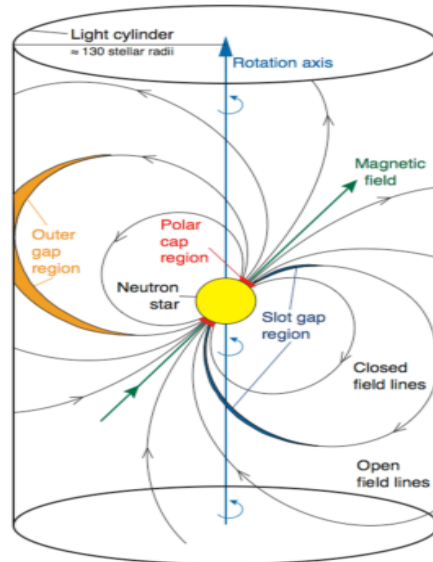


Figure 2-1: Model for the rotating neutron star and its magnetosphere such that the Rotational axis is misaligned with Magnetic axis (refered from Handbook of Pulsars Astronomy.)

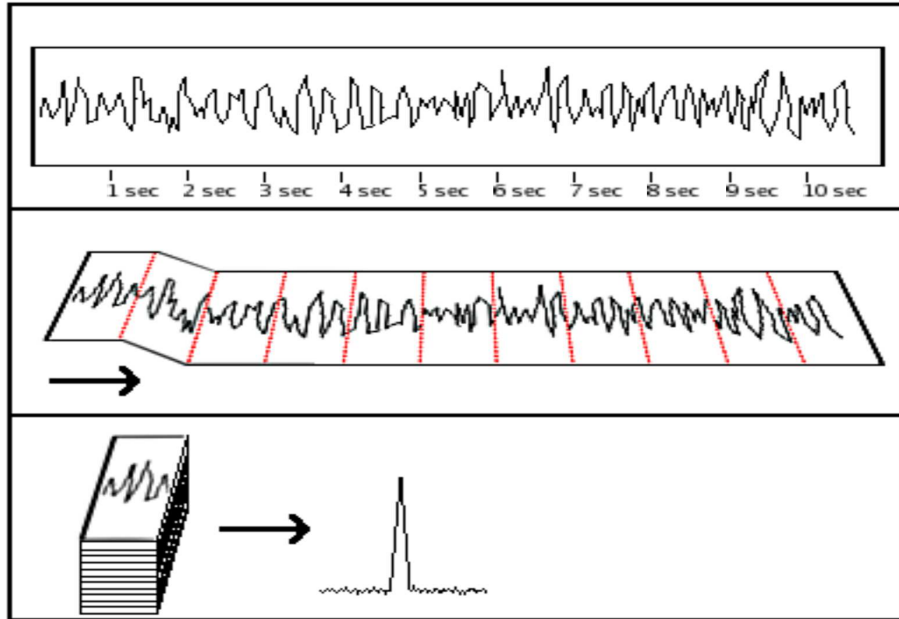


Figure 2-2: An example pulsar with rotation period of 1 second is taken. The pulsar gets stronger with each fold, while the noise strength decreases. (refered from Handbook of Pulsars Astronomy.)

Most of the known pulsar emits radiation in radio frequency range. The unit of Flux Density measured by radio telescope is the Jansky, Jy (where $1\text{Jy} = 10^{-26} \text{ W/m}^2/\text{Hz}$). For pulsars, mean flux density of average profile is a measure of power at that observing Frequency. It has been found that the flux density of pulsars decrease with increase in observing frequency. This dependence can be approximated as $S_{\text{mean}}(f) \propto f^\eta$. Where S_{mean} is mean Flux Density, f is Pulsars observing frequency and η is constant varies for each Pulsar. The flux density, $S_{\text{mean}}(f)$ at an observing frequency is an important parameter for many aspects of Pulsar Astronomy. As well as providing useful constraints on emission mechanism. Drifting subpulses is an another phenomenon for some pulsars where the next subpulse will arrive earlier than the previous one.

2.1 Effects of Interstellar Medium

After leaving pulsars atmosphere, radiation has to travel a long distance before getting detected by our telescopes. During this time, radiation is affected by Inter Stellar Medium (ISM), which can significantly modify our signal and hence need some correction to have a better observation and results.

2.1.1 Dispersion

Ionized gas and free electrons forms interstellar plasma such that net charge is zero. These free electrons and background ions makes its presence felt mainly through propagation effects such as Dispersion. The dispersion relation of electromagnetic waves in a plasma medium can be derived, starting from Maxwell's equations and explicitly including the effect of charges. In the absence of an electromagnetic disturbance, the net charge density in any volume is zero. The incident electromagnetic wave causes polarisation, inducing charge density oscillations. After solving Maxwell's equation we get dielectric constant(ϵ) of plasma as

$$\epsilon = 1 - \frac{\omega_p^2}{\omega^2}$$

where, ω is wave frequency, and characteristic frequency ω_p is given by

$$\omega_p = \sqrt{\frac{n_e e^2}{\pi m_e}}$$

Here, n_e is electron density in the medium, e and m_e is the charge and mass of electron.

The Phase velocity of wave is

$$v_p = \frac{\omega}{k} = \frac{c}{\sqrt{1 - \frac{\omega_p^2}{\omega^2}}}$$

where c is velocity of light and group velocity of wave is given as

$$v_g = \frac{d\omega}{dk} = c \sqrt{1 - \frac{\omega_p^2}{\omega^2}}$$

The propagation speed of a signal is larger at higher frequencies, and approaches c when $\omega_p \ll \omega$.

Hence, The rate of change of arrival time with observing frequency can be measured and

the total dispersion along the line of sight is deduced. If L is the distance of the pulsar then

$$\frac{dt_a}{d\omega} = \frac{4\pi e^2 DM}{m_e c \omega^3}$$

where, $DM = \int_0^L n_e ds$

Measurement of DM can help to determine the average electron density in the line of sight if the distance to the pulsar is known. On the other hand if the average line-of-sight electron density is known, one can use DM to estimate distances of pulsars.

Using this equation we can have difference in time of arrival of two different frequency, emitted simultaneously from pulsar. The time delay is given as

$$\tau = DM \frac{e^2}{2\pi m^e c} \left(\frac{1}{f_1^2} - \frac{1}{f_2^2} \right) \quad (2.1)$$

Here f_1 and f_2 are two different observing Frequency in MHz.

Dispersion causes the low frequency signal to arrive later according to equation 2.1. This will effect the quality of data as the data received at any time sample is not emitted by source simultaneously at every frequency. Therefore to have correct signal at any time sample we need to add time delay to higher frequency with respect to lowest observing frequency. This addition of delays is called as dedispersion of signal and is done by using various methods which are explained in next chapter.

2.2 What is Microstructure?

Rapid intensity modulation in the bright single pulses of pulsars observed with high time resolution is microstructure. Figure 2-3 is one of the single pulses having microstructure emission in it. Here one can see how intensity is changing on short time scale around 1 or 2 ms and quasi-periodicity in the microstructure.

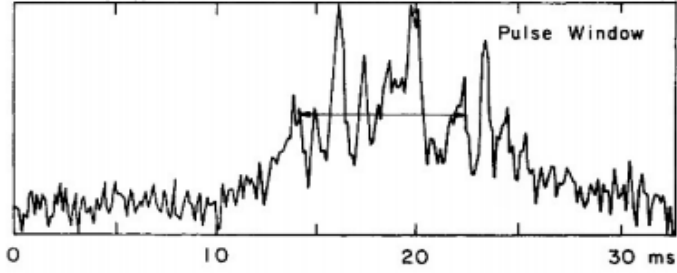


Figure 2-3: A typical single pulse microstructure emission of B2016+28 (referred from Cordes 1990)

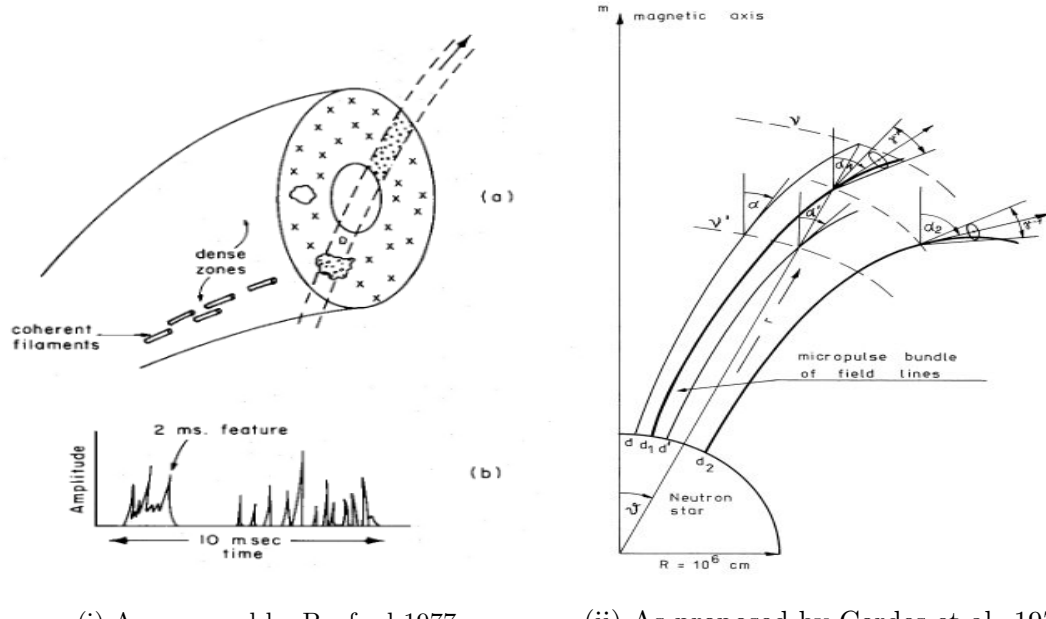
2.3 Microstructure Emission Mechanism

Several attempts have been made in the past to explain the Pulsar Emission Process in Radio Frequency range. One of the most common assumptions as rotating Neutron Star with Dipolar Magnetic Field and emission process is happening in these Magnetic Pole region. A different explanation assumes the neutron Star vibration responsible for microstructure. The modulations of pulse intensity can be interpreted in terms of two models: "temporal modulations" in which the intensity fluctuations are caused by an actual modulation of the radiation beam and "angular beaming" in which the pulsar's rotation sweeps a constant beam across the line-of-sight.

- The first group of model thin flux tubes of plasmas along magnetic field lines carrying charged relativistic particles(Benford et al. 1977). These particles are radiating in their propagation directionand width of the microstructure would corresponds to the angular beaming of these particles. As pulsar rotates these beams will sweep our line of sight and having emission proportional to beam width. It predicts that the broadband nature of the microstructures implies that we are seeing the incoherent addition of many coherent sources.
- The second group of models requires radial structures streaming away from the pulsar along the open field lines, which consist (like in the first group) of charged particles. Higher frequencies emission is then predicted to originate from regions near Polar caps. When they reach a certain height above the pulsar they emit radiation, creating a micropulse with a duration depending on the thickness of the emitting structure (Cordes et al. 1981). The main implication of this paper is that (i) if the subpulse

drift results from the motion of the subbeam around the magnetic axis and (ii) the microstructure is interpreted in terms of the angular beaming model, then the micropulses should not drift consistently with drifting subpulses. The model explains the following properties: microstructure should be less pronounced at high radio frequencies, and the time scale should be frequency independent and proportional to the pulsar period. Also, the micropulses should be symmetrical in shape, and should be broad-band though not as broadband as integrated profiles.

The micropulse time scale, broadband nature and frequency dependence are the parameters which can help us to find restrictions on these models. To estimate the relevance of microstructure, it is important to have a knowledge of microstructure emission in the single pulses of pulsars and to perform analysis on multiple observational frequencies.



(i) As proposed by Benford 1977

(ii) As proposed by Cordes et al. 1971

Figure 2-4: Models for Microstructure Origin

Chapter 3

Signal Processing and Observation Details

The Giant Metrewave Radio Telescope (GMRT), located in Khodad near Pune, India, consists of 30 antennas, each with a diameter of 45 m, spread over a region of 25 km in diameter (Swarup et al., 1997). The array consists of a central array of 14 antennas placed in a Y configuration, along with three arms along the East, West and South directions respectively. The East and South arms consist of 5 antennas, while the West arm consists of 6 antennas. The telescope initially used to operate in 5 frequency bands, corresponding to center frequencies of 150 MHz, 235 MHz, 325 MHz, 610 MHz and 1000-1400 MHz, with a maximum instantaneous bandwidth of 32 MHz. Now, after upgradation it's maximum bandwidth has increased to 400 MHz and various observing frequencies will be modified as 120-250 MHz (for 150 MHz), 250-500 MHz (for 325 MHz), 550-900 (for 610 MHz), 1000-1450 MHz. The feeds provide dual polarisation (circular or linear, depending on the frequency of observation) signals, which are sent to the correlator for beam forming/interferometry. The large extent of the array allows for observations with high spatial resolution in the interferometric (imaging) mode, ranging from 60" at the lowest frequencies to 2" at 1.4 GHz. The high sensitivity of the GMRT at low frequencies, as well as its wide frequency coverage with reasonably large bandwidths also makes it a powerful instrument for pulsar studies.

3.1 Signal Processing for Pulsars Observation

Figure 3-1 shows the components of a signal chain for pulsar observations through a single dish antenna. Starting at the left end, we have the radio antenna, which focusses the radio waves emitted by the astronomical source. The telescope surface is parabolic, with a receiver (which converts the electromagnetic radiation into voltages) at the focus of parabola. After passing through Low Noise Amplifier(LNA) we will downconvert our signal frequency. This is achieved by mixing our signal with signal from a Local Oscillator (LO) at precisely defined frequency. Mathematically which is

$$\cos(\nu_{\text{obs}}) \times \cos(\nu_{\text{LO}}) = \frac{1}{2}(\cos(\nu_{\text{obs}} - \nu_{\text{LO}})t + \cos(\nu_{\text{obs}} + \nu_{\text{LO}})t) \quad (3.1)$$

Now, our signal which is downconverted to Intermediate frequency is again amplified by Amplifier which we can further processed by passing through i) Incoherent Dedispenison system and ii) Coherent Dedispenison Pipeline.

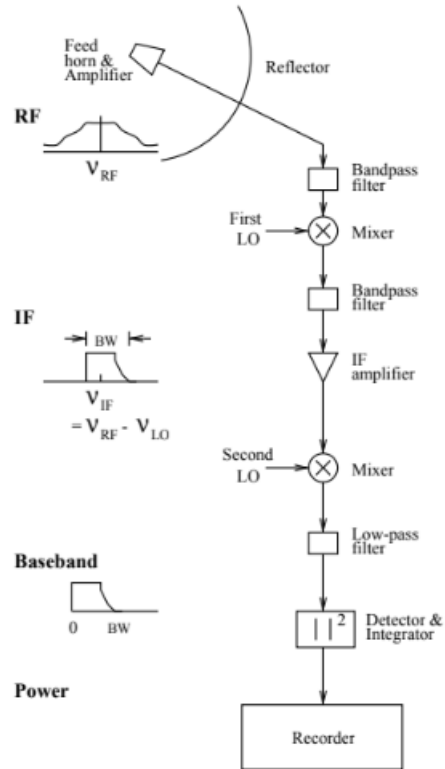


Figure 3-1: Schematic diagram of Radio Telescope Receiver system (refered from Handbook of Pulsar Astronomy)

3.1.1 Incoherent Dedisispersion

There are two types of resolution for pulsar signal. Firstly, time resolution which is required at a level well below the pulse period. Secondly, frequency resolution which is required in order to be able to correct dispersive effect. The easiest means to achieve frequency resolution is to pass the signal through a series of parallel bandpass filters with adjoining frequency responses. Each of these filters creates a single frequency channel, the width of which determines the frequency resolution of our data. The analog power is subsequently sampled in each of these channels, at a given sampling period that determines the time resolution. Finally, the signals of the different channels are shifted in time relative to each other, according to the expected DM delay calculated through Equation

$$\Delta t = 4.15 \times 10^3 DM \left(\frac{1}{\nu_l^2} - \frac{1}{\nu_u^2} \right) ms \quad (3.2)$$

This corrects for the DM delay between the channels, but it is incapable of correcting the smearing within each channel. Therefore if the frequency sub-bands are not narrow enough the dispersion delay may still dominate the signal. Hence we can have narrower frequency band, but this sets limit on the time resolution one can have in the observation or pulse profile. A frequency channel of width $\delta\nu$ will provide independent time sample of resolution $1/\delta\nu$ only. This drawback is corrected with Coherent Dedisispersion method explained in the next subsection.

3.1.2 Coherent Dedisispersion

In previous systems we corrected the relative delay between two frequencies but the smearing itself in the channel is not removed. This can be correct by using coherent method.

The basic signal chain for coherent dedispersion systems is identical upto IF amplifier. Then the signal is downconverted to baseband and subsequently digitised. Next, the signal is Fourier transformed to the frequency domain. The reason for Fourier transforming is that, dispersion is mathematically a convolution process on signal in frequency domain. Using the convolution theorem which states that convolution in time is multiplication in frequency, and deconvolving in Fourier space can be done through division. The frequency

response function characterising the dispersion effects of the ISM is given as

$$H(f_0 + \Delta f) = \exp\left(\frac{i2\pi D(\Delta f)^2 DM}{f_0^2(f_0 + \Delta f)}\right)$$

with f_0 the centre frequency, Δf ($-B/2 < \Delta f < B/2$) the offset from the centre frequency and D the dispersion constant. Removal of the dispersive effects can easily be done by dividing the Fourier transform of the signal by this function. Now, by following Inverse Fourier Transform of our signal, we will get our original signal in time domain.

The steps involved in coherent dedispersion are now clear:

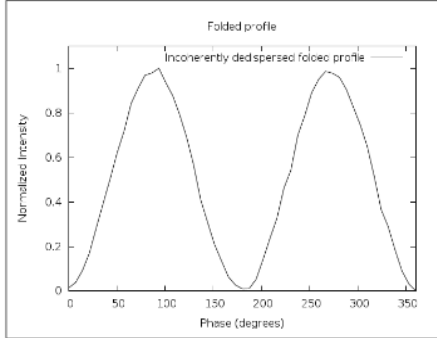
- 1) Obtain a time series by sampling the baseband voltage $V(t)$ at the Nyquist rate (sample rate = $1/(2 \times \text{the bandwidth})$).
- 2) Fourier transform the time series to the frequency domain. This yields

$$V(\nu)_{\text{detected}} = V(\nu)_{\text{emitted}} H(\nu)$$

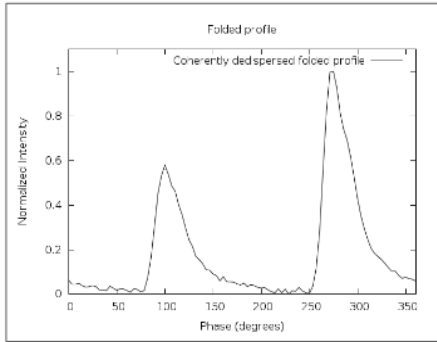
- 3) Multiply the above spectrum by $H^{-1}(\nu)$, to obtain $V(\nu)_{\text{emitted}}$ which is our original signal emitted by source.

- 4) Inverse Fourier transform back to time domain to obtain the corrected voltage time series $V_{\text{emitted}}(t)$. This is now free of in-band dispersion. This voltage can now be passed through a detector.

Comparison of Coherent and Incoherent Dedisperion is given in Figure 3-2. The effects of intra-channel dispersion timeare clearly evident in terms of smearing of the folded profile in the incoherently dedispersed case, whereas, the coherently dedispersed pulse profile is narrowed and shows clear indication of a scattering.



(a) Incoherently dedispersed and normalized folded profile for B1937+21.



(b) Coherently dedispersed and normalized folded profile for B1937+21.

Figure 3-2: Incoherently and coherently dedispersed normalized folded profiles of the pulsar B1937+21 observed with the GMRT at 325 MHz. The pulsar has a period of 1.55 ms and a DM of 71 pc/cc. (Source: Kishalay De and Yashwant Gupta, 2015)

3.2 Observation Details

The Sub-Array mode of the GMRT allows one to combine only a specific set of antennas into a single array, while using the rest (or a subset of it) as another array. This allows one to carry out simultaneous dual-frequency observations of a variety of radio sources for achieving different kinds of science goals. In our case, the two sub-arrays can be tied to two different back-ends configured at two separate frequencies, to receive total intensity (or full Stokes) signals from these frequency bands. This will allow us to explore the characteristics of micropulses simultaneously at two different frequencies. These observations were carried out during May and July of 2016. The observing configuration involves one sub-array tied to the GSB (GMRT Software Backend) at 325 MHz with 32 MHz bandwidth and integration interval as $15\mu\text{s}$, along with another sub-array attached to the GWB (GMRT Wide Backend) at 610 MHz with 100 MHz BW. Use of coherent dedispersion with the GSB will

allow high time resolution observations, while the GWB PA mode with $40\mu\text{s}$ time resolution and 1K frequency channels would be enough to correct for dispersive effects at 610 MHz.

3.3 Candidate Selection

The set of Pulsars for this study purpose is carefully chosen depending upon i) previously reported Microstructure studies, ii) Higher SNR for single pulse detection and iii) Low Dispersion measure so it won't affect our time resolution and provide us maximum possible time resolution. Based on these criteria we are presenting the full list of Observed Pulsars during GMRT Observation Proposal 30_074.

Pulsar	Period (ms)	Flux(400 MHz) mJy	Flux(600 MHz) mJy	DM (pc cm^{-3})
B0329+54	714.5196	1500	1300	26.776
B0950+08	253.0651	400	103	2.96
B1642-03	387.68	393	173	35.75
B2016+28	557.95	314	101	14.19

Table 3.1: List of Pulsar observed under proposal along with their know parameters(all the values Flux, Period and DM are taken from ATNF Pulsar Catalogue).

3.4 Microstructure Properties at Dual Frequency

For most pulsars, the pulse profile is often a function of observing frequency due to a number of intrinsic effects (e.g., emission location in the pulsar magnetosphere) and extrinsic effects (i.e. dispersion in ISM), see e.g. Cordes (1978). This leads to pulse broadening and component separation when we move to the lower frequencies. The same phenomenon is also seen in the subpulses. However, the microstructures generally do not show this kind of behaviour.

The characteristics of micropulses have been scarcely explored with multifrequency observations in the past (e.g. Boriakoff, 1983) and thus holds the potential for revealing many unknown aspects of microstructure emission. The limited number of previous studies (primarily done with the Arecibo telescope) have indicated that microstructure emission is intrinsically broadband, and does not follow the traditional Radius to Frequency Mapping

model observed in subpulses (e.g. Boriakoff, 1983; see Gil, 1986 for a relevant model). Boriakoff studied the pulsar B1133+16 simultaneously at 196.3 and 318 MHz, and found that i) micropulses have a steeper spectrum than the average profile, with the spectral index varying across the pulse longitude phase, and ii) the microstructure widths themselves have a very flat spectrum, and do not show any significant frequency evolution. However, almost all of these studies were done on a small set of pulsars, with most of the detailed studies being done on PSR B1133+16 due to its high flux and low DM. Such properties are best explored with simultaneous dual frequency observations, and is thus ideally suited for a multi-element telescope like the GMRT. Our simultaneous multi-frequency observations have indicated that single pulses often show similar structures at these widely separated frequencies.

3.4.1 Folded profiles and Individual pulses of B2016+28 and B0950+08

We have observed single pulses from various pulsars simultaneous at Low Frequency i.e. 325 MHz and High Frequency i.e. 610 MHz. The following figures show the folded profile of two of them B2016+28 and B0950+08.

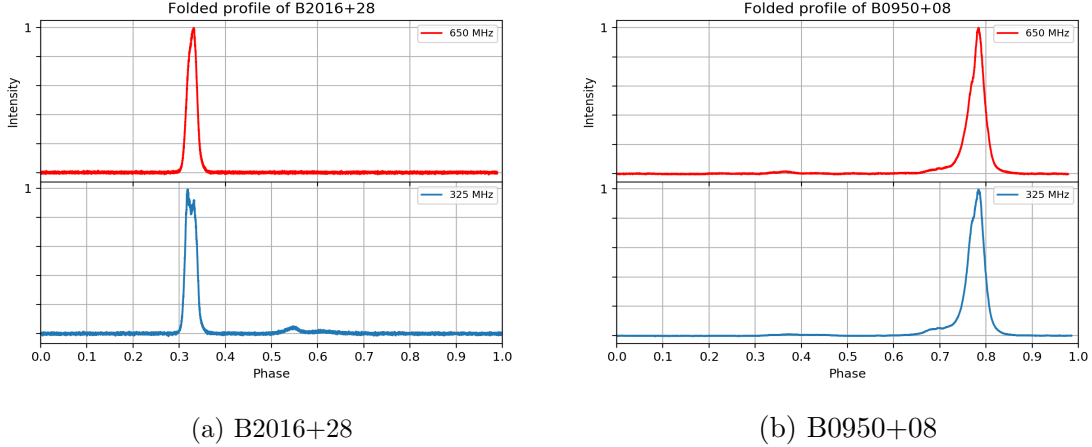


Figure 3-3: Folded profiles

The emission for B2016+28 is seen to be constricted in the phase of 0.31 to 0.36 and that for B0950+08 to in between the phase of 0.74 to 0.82. Thus we should see all the emissions from pulsar (subpulse and microstructure) in between these phases. For further discussions, we will zoom into these phases and perform all our analysis on them. We show an example pulse, from the B2016+28 and B0950+08 pulsars, in order to demonstrate the

rich variety of microstructure discovered through our analysis.

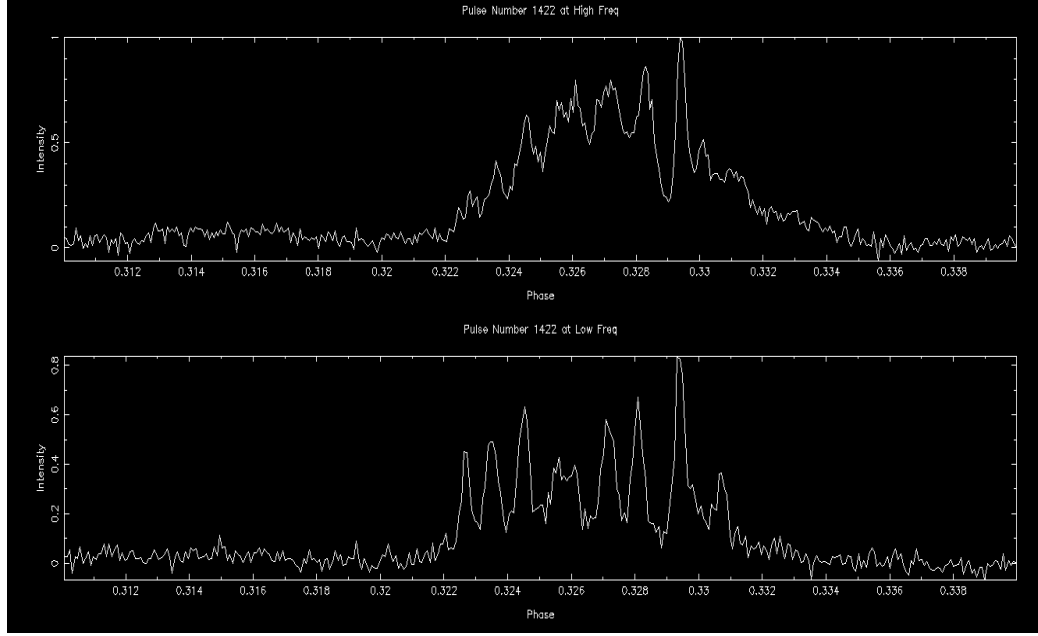


Figure 3-4: A single pulse of B2016+28 showing the emission of microstructure riding on a smooth pulse between the phase of 0.31 to 0.34

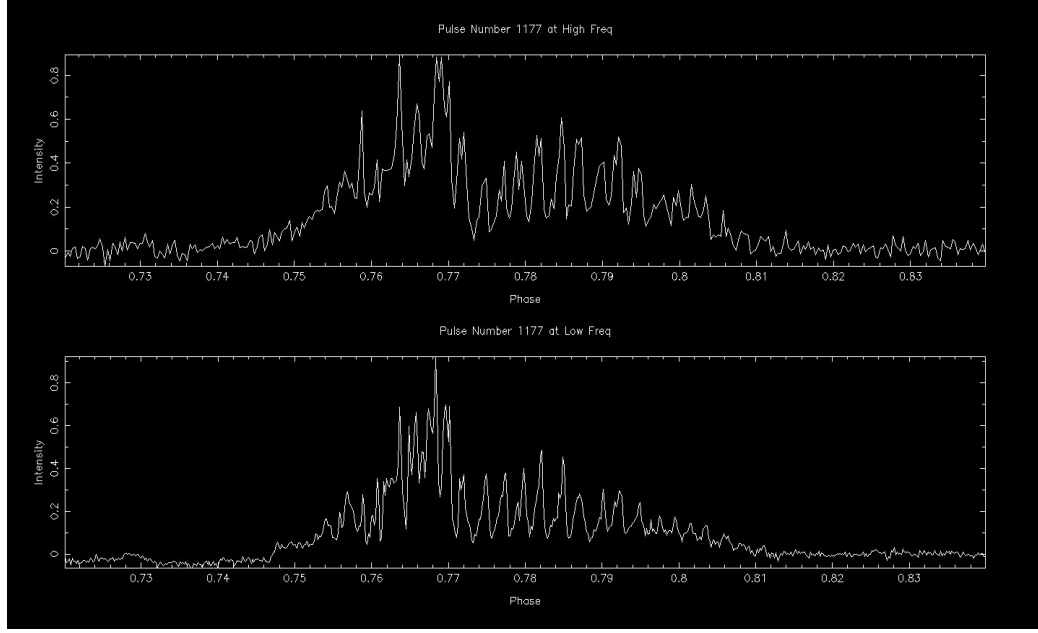


Figure 3-5: A single pulse of B0950+08 showing the emission of microstructure riding on a smooth pulse between the phase of 0.74 to 0.82

B2016+28: This is one of the drifting pulsar from our list of observation studied for its microstructure properties many times in past. Observed microstructure emission are deep

intensity fluctuation over weak subpulse and quasi periodic microstructure. Here the general trend is to see stronger microemissions for the lower frequency and stronger modulating subpulse for the higher frequency. One can see that the folded profile at higher frequency has a smoothed single component, but at lower frequency it is splitting into two different component.

B0950+08: This pulsar is again one of the example of wide variety of microstructure emission. Most of the micropulses are quasi-periodic in nature and some very narrowed like an unresolved single spikes. The folded profile at low frequency is broader than at high frequency.

One would now like to have a tool to browse through single pulses in data sample to visually look for interesting single pulses showing microstructure. We highlight some aspects of the analysis of single pulses in the next two chapters.

Chapter 4

Data Analysis and Algorithms

As mentioned in the previous Chapter simultaneous dual frequency observations are carried out using the GMRT at 325 MHz and 610 MHz. Due to large number of single pulses, it is very hectic to study each single pulse and characterize the microstructure. Hence a new algorithm is developed which can detect and characterize microstructure. Initial parts of the code was written in 'C' by Kishalay De (De et al. 2016, 2015) under his Masters project thesis, where one can browse through the individual pulses at both frequency and characterize them. The code itself has now evolved to have a number of very useful features, including those required for data analysis. It can now perform analysis to get the width, period, power, autocorrelation function, and cross correlation function of a given pulse at both the frequencies. The most important feature of this algorithm is that it can detect and characterize microstructure for all the available pulses in the data set one by one continuously and store the calculated quantities of interest in a text file, this process is named as Automated Analysis. Here we have explained the features of our algorithm and how it is characterizing the individual pulse.

4.1 Autocorrelation Analysis

The Autocorrelation Function (ACF) is a very useful tool to detect and estimate widths of any quasi-periodic phenomenon(Cordes et. al 1976, Lange et. al 1998). Many of the previously reported Microstructure properties used ACF to characterize it. The intensity data comprises of three components: white noise, subpulse and microstructure riding on it. The autocorrelation of a continuous-time white noise signal will behave like a Dirac

delta function at $\tau = 0$ and is negligible for all other τ . As shown in Figure 4-1 various timescale can be obtained from ACF of single pulse. Here we are interested in the width of Microstructure, and periodicities. For an array $a(i)$ of size N , the ACF is defined as

$$ACF(\tau) = \sum_{i=1}^N \frac{a(i)a(i + \tau)}{a(i)a(i)}, \quad \text{if } i+\tau \leq N \quad (4.1a)$$

$$ACF(\tau) = \sum_{i=1}^N \frac{a(i)a(i + \tau - N)}{a(i)a(i)} \quad \text{otherwise} \quad (4.1b)$$

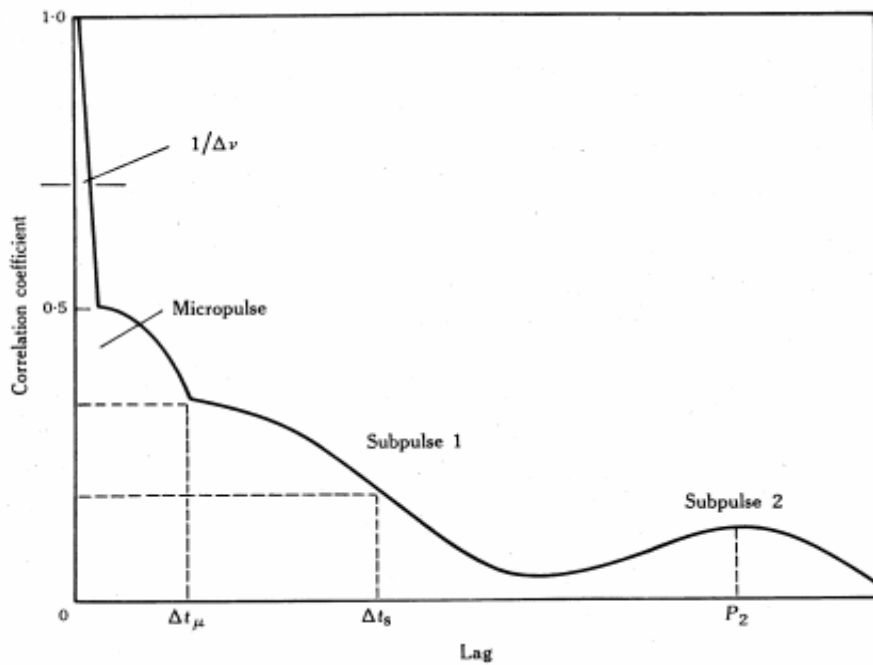


Figure 4-1: Schematic of Autocorrelation Function (ACF) of a pulse is shown. Here Δt_μ is micropulse break point and Δt_s is half-width at half-maximum. The narrow spike of width Δt is due to noise in the signal. (refered from article on Pulsars Microstructure by J. M. Cordes 1979)

4.1.1 When does the Autocorrelation Function (ACF) fail?

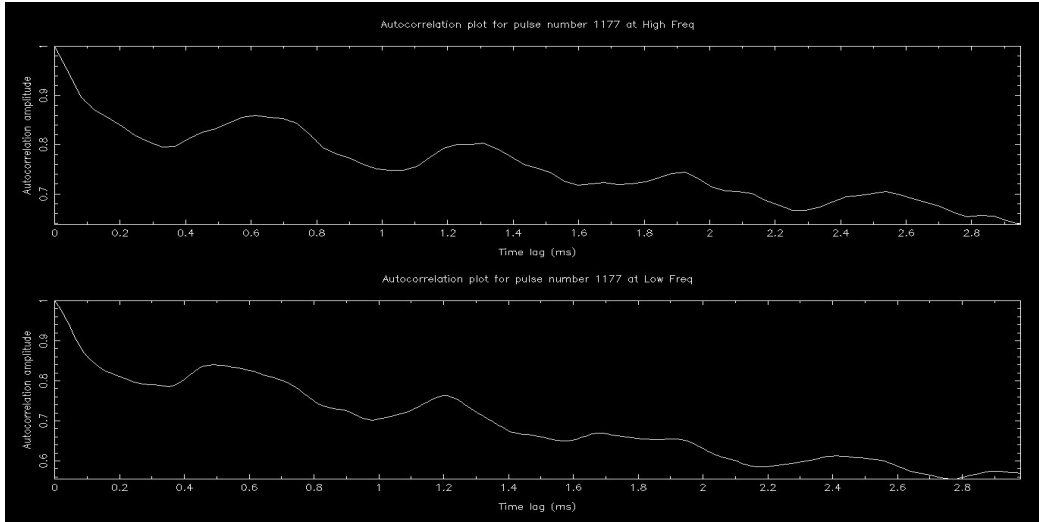


Figure 4-2: ACF of the pulse from B0950+08 shown in the figure 3-5

The Autocorrelation Function of a pulse plotted for B0950+08, in figure 3-5, is shown in above. This pulse is showing prominent microstructure emission, but one can see that ACF is barely showing any microstructure evidence. The micropulse is comparatively weaker as compared to subpulse power, therefore subpulse is dominating in the ACF. We can see even if there is microstructure present in the single pulse, it is hard to make any characterization from single pulse ACF. Hence we need a different analysis technique to do better micropulse study. The next section deals with the new analysis process and its effect on the micropulse.

4.2 Smoothed Subtraction: Extracting only microstructure feature from the subpulse

The ACF shown above has microstructure which produces a periodic maxima, all these structure is riding over a broad subpulse envelope which is peaked over 0 time lag. In most pulses, the subpulse can be stronger than the microstrucure feature and mask these periodic maxima of the ACF by smoothing them. So, one has to take care that this subpulse is not affecting our widths and period estimates.

This is done by separating microstrucure emission from the subpulse by using the fact that

microstructure are intensity modulation at milliseconds scale. Separation of microstructure is achieved by using moving boxcar average method. We use a Where we can use desired box size(later this box size is called as Smoothing Window) such that its size is more than microstructure size, so micropulse is preserved. We can smooth the single pulses and the smoothed part is considered as the broad subpulse envelope over which microstructure is riding. Now, we subtract this smoothed single pulse from the original single pulse and the remaining part (*residual pulse*) is just the microstructure. Mathematically, we have single pulse signal as $p(i)$ and the calculated smoothed single pulse signal as $s(i)$. Then, the microstructure feature $m(i)$ is obtained by subtracting $s(i)$ from $p(i)$ as

$$m(i) = p(i) - s(i) \quad (4.2)$$

where, i corresponds to data point of single pulse.

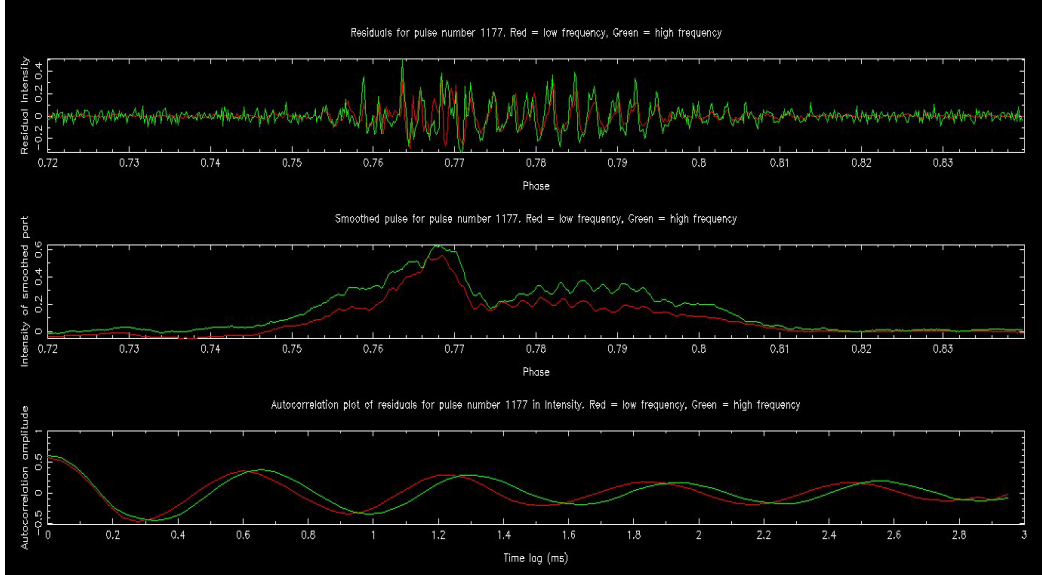


Figure 4-3: Top plot is showing a single pulse of B0950+08 at 325MHz(Red) and 610MHz(Green). Middle plot is the smoothed pulse. Bottom plot is showing the residual Micropulse obtained after subtraction of smoothed pulse from single pulse. The bottom figure shows the ACF of the residuals.

We can see that the residual microstruture feature $m(i)$ of the pulse no. 1177 in the Figure 4-3 after subtraction of smoothed subpulse from single pulse. The Residual has improved the micropulse phenomenon and maintained most of its structure. The ACF of

this residual Figure 4-3 is distinctively shows the periodic maxima, which were not clearly visible in the single pulse ACF Figure 4-2. This technique has improved the micropulse signal, such that it becomes easier to analyze them.

4.3 Microstructure Detection

We have the extracted microstructure emission feature from the single pulse of pulsar and it has to be decided whether the extracted micropulse is really showing microstructure or it is just noise. Note that the residual $m(i)$ often has some small part of subpulse retained from the main single pulse which can be seen in the ACF also. Here we are addressing the criteria which individual single pulse residual should follow to have reliable microstructure in it. We have used Root Mean Square (RMS) of the residual to detect micopulse feature. One has to take care of the Off Pulse noise of Pulsar, such that it is not contributing in the RMS. Hence we define that pulse has microstructure if,

$$\begin{aligned} \frac{RMS(m(i))}{RMS(o(i))} &> 3 & \text{or} \\ \frac{\text{maximum}|m(i)|}{RMS(o(i))} &> 10 \end{aligned} \quad (4.3)$$

where,

$$RMS(m(i)) = \sqrt{\frac{\sum_{i=0}^{N_{on}} m(i)^2}{N_{on}}}$$

and

$$RMS(o(i)) = \sqrt{\frac{\sum_{i=0}^{N_{off}} o(i)^2}{N_{off}}}$$

Here N_{on} and N_{off} is the number of sample points in the ON Pulse and OFF Pulse of particular single pulse of Pulsar. The OFF Pulse region is specified during the start of the Analysis routine from the folded profile of pulsar and ON Pulse region is of our choice over one would like to run the desired analysis routine. A given residual pulse is classified as having microstructure when it satisfies the above mentioned criteria 4.3. Once we

have classified the given single pulse residual as having microstructure we proceed for its characterization like width, period, power etc. The smoothed subtraction analysis method is advantageous as compared to previous single pulse ACF method, it gives us weak micropulses of the single pulse. With condition 4.3 we can have a better residual micropulses for analysis. It is to be noted that this criteria can be changed during Automated Analysis.

4.4 Analysis Configuration and Changes

We have to use certain optimum condition during micropulse analysis as they are able to affect our results. First of all the OFF pulse region from average profile should not have any significant noise in it. The microstructure detection criteria equation 4.3 depends on OFF pulse RMS, hence any contribution from noise may mask detection.

Smoothing window size i.e. size of box for smoothed subpulse calculation using moving boxcar average method is another important criteria and it is that part which made our analysis easier. One has to use optimum smoothing window for subpulse subtraction. This can be fixed by using various trial smoothing window sizes and then visually decide which one of them is able to subtract subpulse with maximum micropulse fluctuation retained in the residual pulse. But, one has to be careful about smoothing window size because it is observed that using higher window size leads to higher estimates of widths and period as compared to lower window size (Mitra et al. 2015). The size of smoothing window can be different for every pulsar and sometimes for same pulses at two different frequency. Here for all the results presented in this we used 1ms as smoothing window size for all pulsars.

4.5 Microstructure Widths

The Autocorrelation Function of the residual micropulse Figure 4-3 provides useful information about the width of the individual single pulses microstructure. The ACF has a normalised peak of squared magnitude of all the residual data points at zero lag and as time lag increases the structure decorrelates and then there is sharp decrease in the ACF when the time lag is less than the width of the particular structure. When time lag becomes

more than the widths of feature at this point the two pulses separate out and the ACF becomes almost flat. As we keep on increasing the time lag the micropulse correlates again and we get a peak in ACF and this is repeated as per the micropulse structure. Notice the next peak of the ACF is just more than zero ACF amplitude and with time lag slowly decays and becomes flat with zero ACF amplitude, at this time lag the micropulses time lag is beyond subpulse width. Hence the pulses are no more correlated, therefore ACF is almost zero.

Width of the residual micropulse $m(i)$ is calculated as follows, At zero lag there is a contribution from noise in the micropulse as shown in Figure 4.1. We expect that the noise is having a white spectrum so it decorrelates as soon as you increase the lag and one can see it did decorrelate in the ACF shown above. So we look for the time lag at which ACF is half of its amplitude at the very first time lag sample instead of zero time lag, so we can also exclude the contribution from noise. We define this time lag as half width of the micropulse and report twice this lag as the width of micropulse feature.

4.6 Microstructure Periodicity

Previous reported studies(Cordes et al. 1976) used Mainly ACF of micropulse to estimates the periodicity in it. They simply estimate the first peak in the ACF and report this as the period of micropulse. But, ACF has a number of contribution from many sources where one important factor is the subpulse which is strong enough to mask quasi-periodicity of micropulse. So, one would like to have a better and reliable periodicity estimates.

We already have the extracted micropulse feature from a single pulse Figure 4-3and can easily search for the periodicities in the Frequency domain. We can use this advantage and calculate the power spectrum of this residual micropulse those which are satifying the microstructure criteria. Here one is looking for a local maxima in the power spectrum of the micropulse such that the peak power is greater than the OFF pulse power. We define the period of micropulse as

$$P(i-2) < P(i-1) < P(i) > P(i+1) > P(i+2) \quad (4.4)$$

where, $P(i)$ corresponds to the data point of Power Spectrum. This is the 5 point local maxima condition must be satisfied by any $P(i)$. Once it passes this, then next condition checks the power contained in this frequency bin and provides us following condition on power

$$P(i) > 3 * RMS(P(i)) \quad (4.5)$$

The data point which satisfies both of the condition 4.4 and 4.5 is the preferred Period of micropulse. Due to quasi-periodicity of micropulse there can be more than one point satisfying these conditions, so we chose the point with maximum Frequency. Hence we have smallest period of micropulse. If there is any point before Power Spectrum Frequency cutoff value obtained from average ACF as average width, this point is not considered.

While for period detection we are using Power Spectrum of residual micropulse calculated from FFT algorithm. During component analysis the residual micropulse pulse has less number of data points as compared to Full ON single pulse especially for component analysis. Therefore, the power spectrum of these micropulses has less number of data points in it. The direct consequence of this is we lose resolution in frequency domain, sometimes this can affect our period detection when it can not satisfy equation 4.4. Period detection process require a cutoff frequency or avg width of subpulse, this cutoff frequency is calculated from the average ACF of all the pulses. The half width of the ACF neglecting contribution from noise is the avg width of subpulse as shown in Figure 4-1. This avg width is not same at two frequency this caused abrupt decline in period values due to different cutoff frequency. This issue is solved by using higher avg width among them so periods have same cutoff.

4.7 Cross Correlation Analysis

The pulsar emission is a broadband phenomenon i.e. it emits at multiple frequencies. After aligning the subpulses at two frequencies, with the correct dispersive measure, we see that the microstructures still have some time lag between them. (see section: 3.4). To quantify this non-alignment of microstructure emission, we use normalised cross-correlation function (CCF) on the signals which gives a measure of similarity of two time-series as a function

of the displacement(time-lag) of one relative to the other. A graphical representation can be seen by clicking this [link](#) (Source: Wikimedia Commons). The function takes the value from (-1,1) depending upon the how closely the time-series match at different lags. For the given arrays (x_i, y_i) of length N , with mean as (\bar{x}, \bar{y}) and standard deviation as (σ_x, σ_y) , the measure of strength of the correlation is given by the correlation coefficient (r):

$$r = 1/N * \frac{\sum_{i=0}^N [x(i) - \bar{x}][y(i) - \bar{y}]}{\sigma_x \cdot \sigma_y}$$

When the residuals are perfectly correlated, $r = 1$. If they are perfectly anticorrelated, $r = -1$. If they are completely uncorrelated, $r = 0$.

4.7.1 CCF on the residuals

We take the residuals of pulse whenever microstructure detection is on both the observational frequencies. A simpler picture of CCF can be thought as keeping one of array fixed and sliding the other array in time axis, then calculating the integrated product of the two arrays. For discretely sampled data, such as ours, this implies that the sampling interval of both the arrays should be the same. Since the sampling interval of respective frequency is different ($15.36\mu s$ at 325 MHz, and $40.96\mu s$ at 610 MHz), we have to reconstruct the data-sets in order to have the same sampling size. The process of achieving it is described in the following sub-section.

Matching the resolution at both the frequencies

We integrate $15.36\mu s$ sampled data to $46.08\mu s$ such that the three consecutive bins are averaged to give a value. Then we resample the the $40.96\mu s$ data to $46.08\mu s$ using the linear interpolation. Say (x_a, y_a) and (x_b, y_b) , is to interpolated to point (x,y); then the interpolant is given by:

$$y = y_a + (y_b - y_a) \frac{x - x_a}{x_b - x_a}$$

The CCF of the resulting residuals is then calculated to give a normalised CCF vs time-lag data. The CCF of one such pulse (refer: sec3.4) is plotted below. We see oscillating peaks in

the graph which signifies the periodic nature of the microstructure on both the frequencies. We consider the x-axis point corresponding to the nearest peak of the CCF as the time-lag between the micropulses at two frequencies. We will now refer to the shift in time-lag in terms of bins, where **1 bin = 46.08 μ s**.

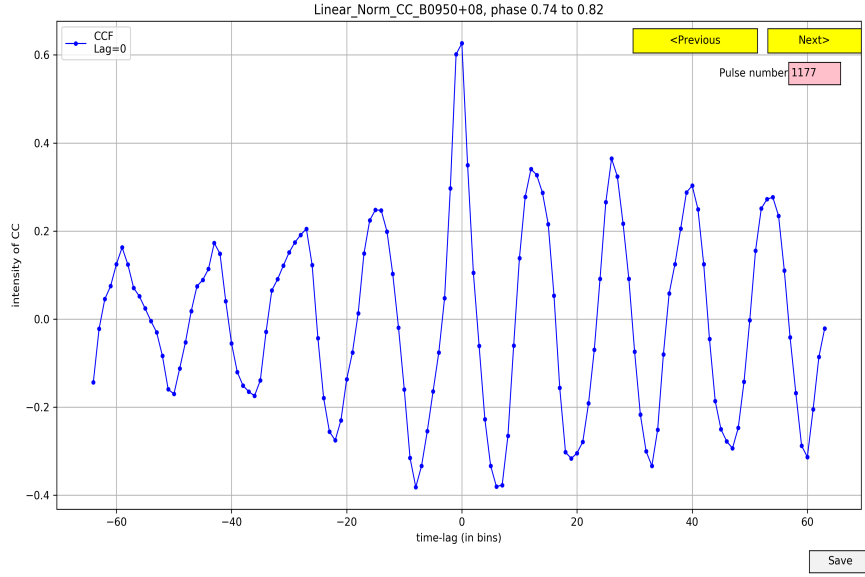


Figure 4-4: The CCF plot for the pulse shown in fig 3-5. Time-lag from the graph = 0 bin (Here, 1 time-bin=0.04608ms)

4.7.2 Interpolating the CCF peak

We note that the minimum shift that can be detected with the above routine, is bounded by how the data is sampled (here, 46 μ s). Thus, if the actual shift is smaller than one bin or is some fraction(say 2.55), the CCF will report a flat peak. For example, as calculated by manual inspection (i.e. by zooming into phases and noting the alignment between the peaks of micropulse train), the time-lag between the two pulses shown in fig 3-5 should be around -0.4392bins. But the fig 4-4 shows that there is a flat peak between -1 and 0 time lag. The nature of the peak depends on how closely the microstrucutre train matches as we shift from one time-lag to the next one. We can use this property to better estimate the CCF by doing a polynomial fit of the points near to the reported peak. This is achieved by taking the neighbouring 5 points on each side (11 points in total) of the peak and doing a 7 degree polynomial fit. The fitted graph is plotted in the following figure:

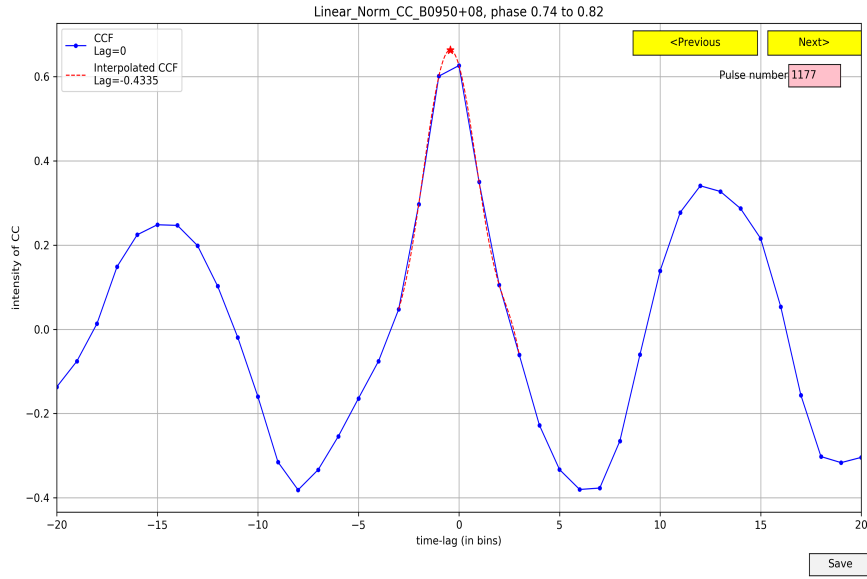
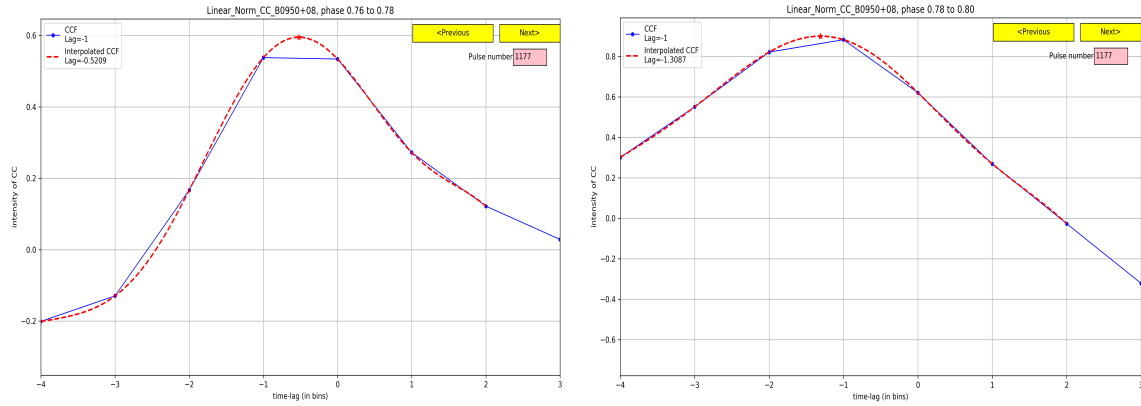


Figure 4-5: The polynomial fitted CCF plot for the fig 4-4. We note that the reported value of -0.4335 bins is in a good agreement with the manual inspected value of -0.4392 bins

4.7.3 Dependence of CCF on the phase window

Consider the pulse of B0950+08 and its corresponding CCF plot, in the last section. The interpolated peak shows a lag of -0.4335 when seen in the phase range of "0.74 to 0.82". Since the pulse train is extended in a long phase window we can now split the bigger phase and calculate the CCF for a narrower window. In the following figure we plot the CCF of the same pulse with a different phase windows of "0.76 to 0.78" and "0.78 to 0.80":



(i) Phase window of 0.76 to 0.78

(ii) Phase window of 0.78 to 0.80

Figure 4-6: CCF plots for a pulse with different phase windows

We notice that the interpolated time lag reported for the two phases change from ”-0.5209” (*in 0.76 to 0.78*) to ”-1.3087” (*in 0.76 to 0.78*). This implies that there might be a phase/window dependence of the microstructure alignment at two given frequencies.

We can probe this nature by doing the following excercises:

- To divide the bigger phase into smaller windows.
- Check if the microstructure train is present in multiple phases. This can be achieved by getting common pulses in any two or more phases windows(on which microstructures were found on both the microstruture).
- Then plotting the distribution of the interpolated CCF for the given phase and note the mean time-lag.
- Thus if we see a change into the alignment, i.e. mean, as we move across the phases, it would mean that the lag of the microstrucutre depends upon the phase range being zoomed in.

We carried out the analysis in B2016+28 and B0950+08. In the former pulsar, only the first point has been implemented; whereas all the mentioned excercise were performed for B0950+08 case. The resulting plots are shown in next chapter.

Chapter 5

Micropulse Statistics and Results

In the previous chapters, we developed the framework for various automated data analysis associated with microstructure emission. The methodology has been to first look at a particular pulsar, then pick an individual sub-pulse, check whether it crosses micro-structure cut-offs. In case it does, then we derive the residual pulse by smoothening (SG algorithm), and then find the width and the quasi-periodicity by the earlier discussed methods. This chapter presents the results of these analyses for the various pulsars in our observing campaign. In the following analysis, the LF(GSB) sampling interval has been set to 3 sample points integration. This is used for comparable time resolution at both frequency. The smoothing window size of 1 ms is used for all the pulsars, as it is found to optimum value.

5.1 Width Distribution

Histograms of the statistical distribution of micropulse widths detected in single pulse at 325 MHz (LF) and 610 MHz (HF) were plotted. These Histograms are quantified by calculating each pulsars width distribution mean(μ) which gives us the preferred widths of micropulse and Root Mean Square Deviation (RMS) to get an estimate of typical spread in each distribution as given in the table.

5.2 Period Distribution

As described earlier, the periodicity of the individual residual pulse (given that microstructure is present) is calculated by the picking a frequency peak according to the eq. 4.4.

In the automated analysis, the detected period is stored in a .txt file. We then plot the histogram for the given pulsar to get the micropulse period distribution. The mean and the standard distribution of the histogram is mentioned to get an estimate of typical spread in each distribution, as given in the following table.

Histograms for the Width of the Microstructures

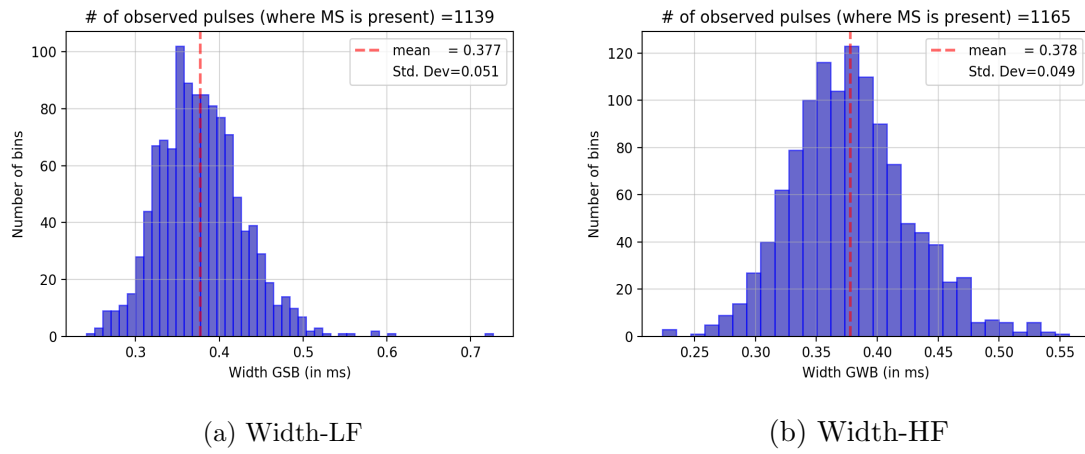


Figure 5-1: For pulsar B0329+54

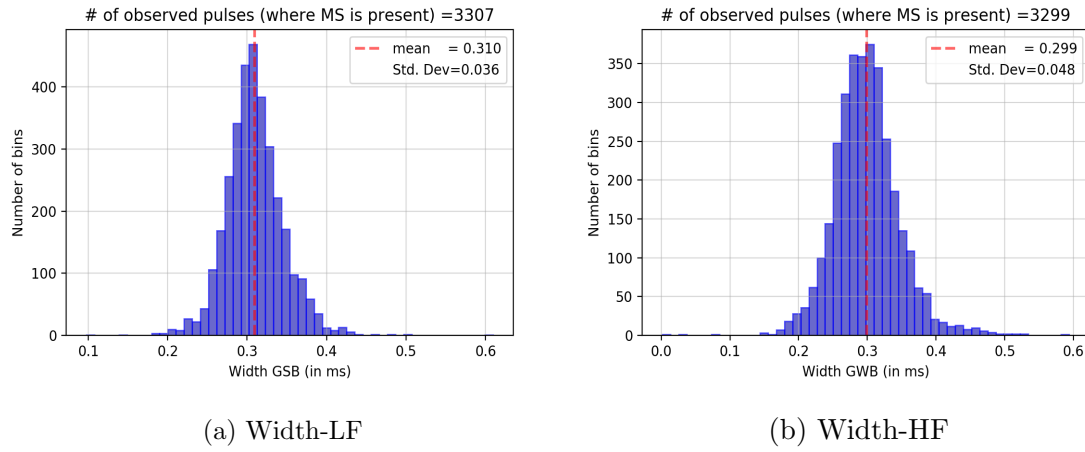


Figure 5-2: For pulsar B0950+08

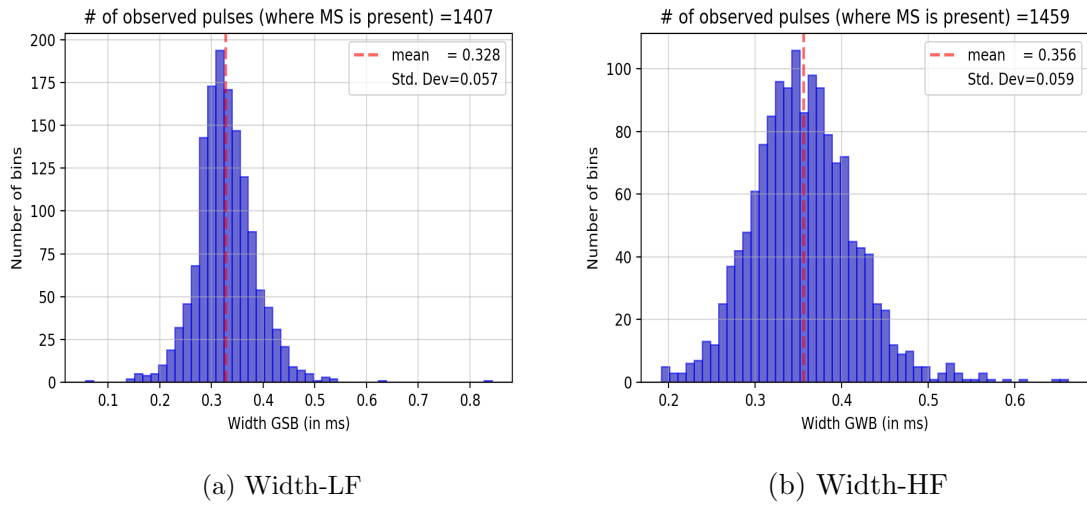


Figure 5-3: For pulsar B1642-03

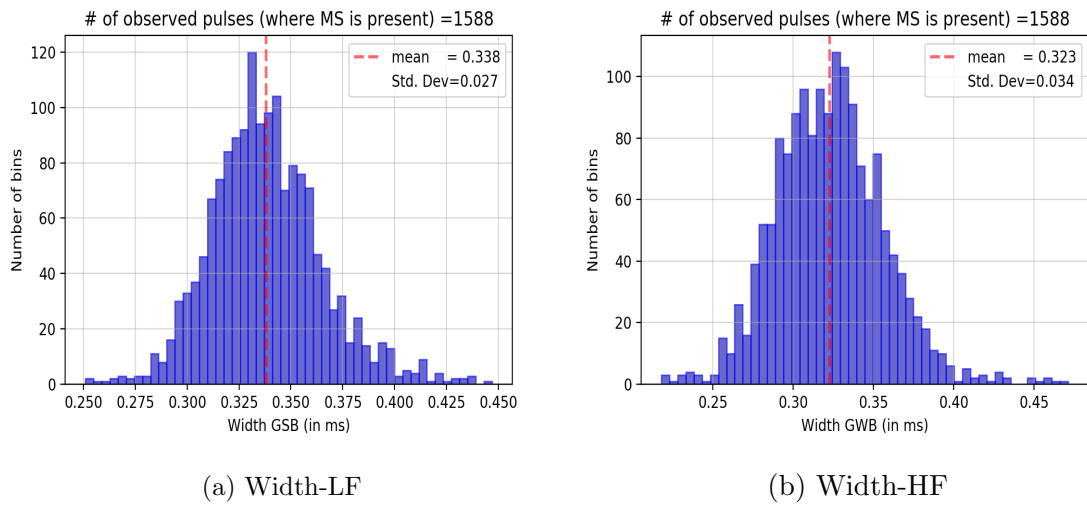


Figure 5-4: For pulsar B2016+28

Histograms for the Period of the Microstructures

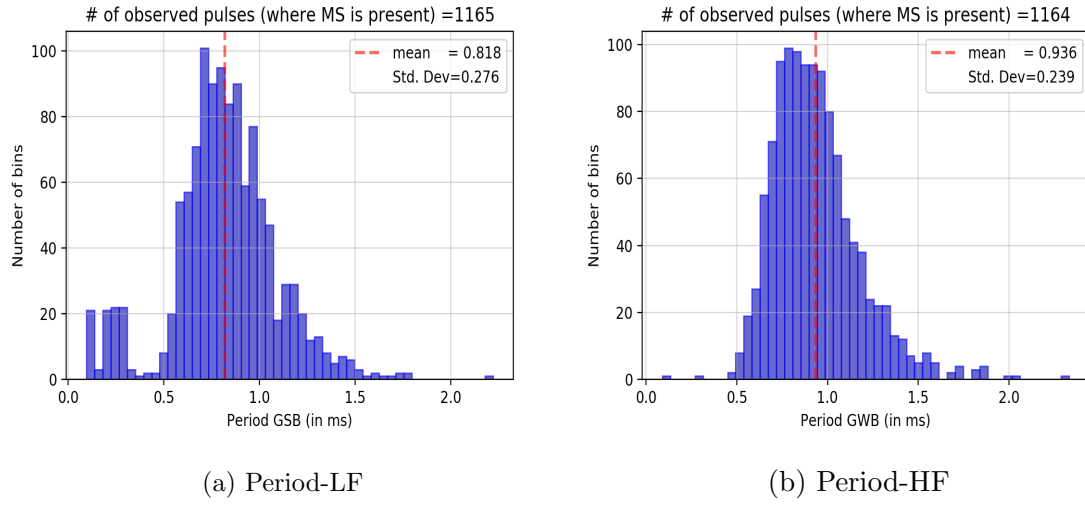


Figure 5-5: For pulsar B0329+54

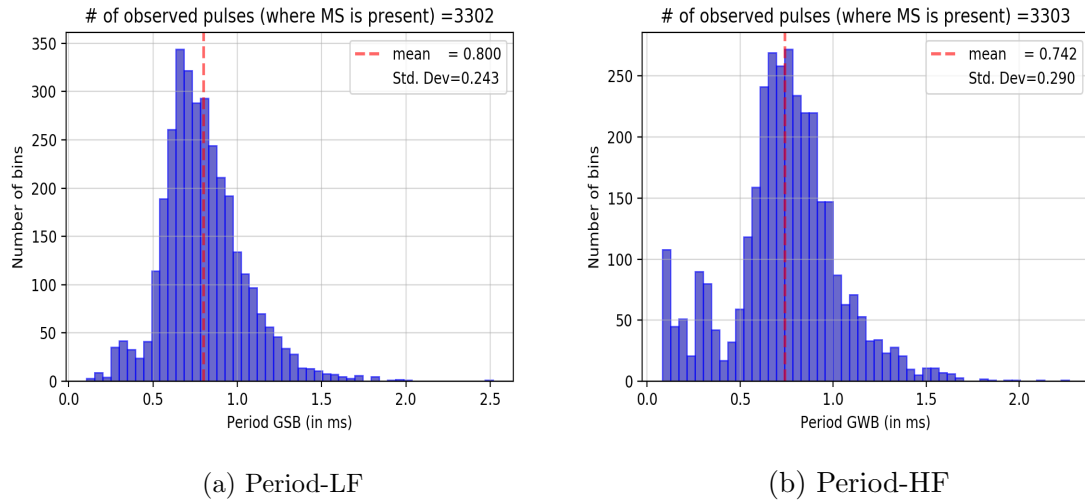


Figure 5-6: For pulsar B0950+08

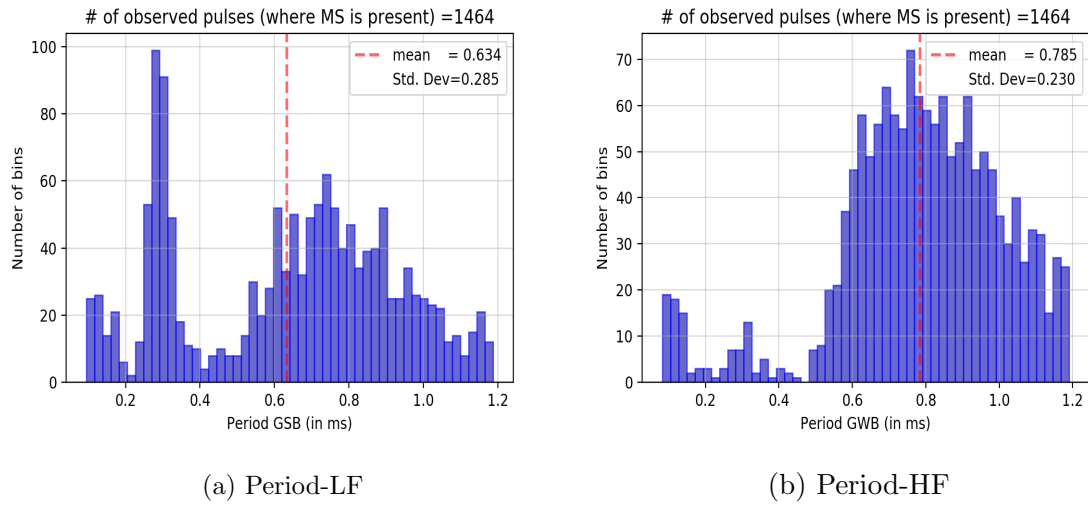


Figure 5-7: For pulsar B1642-03

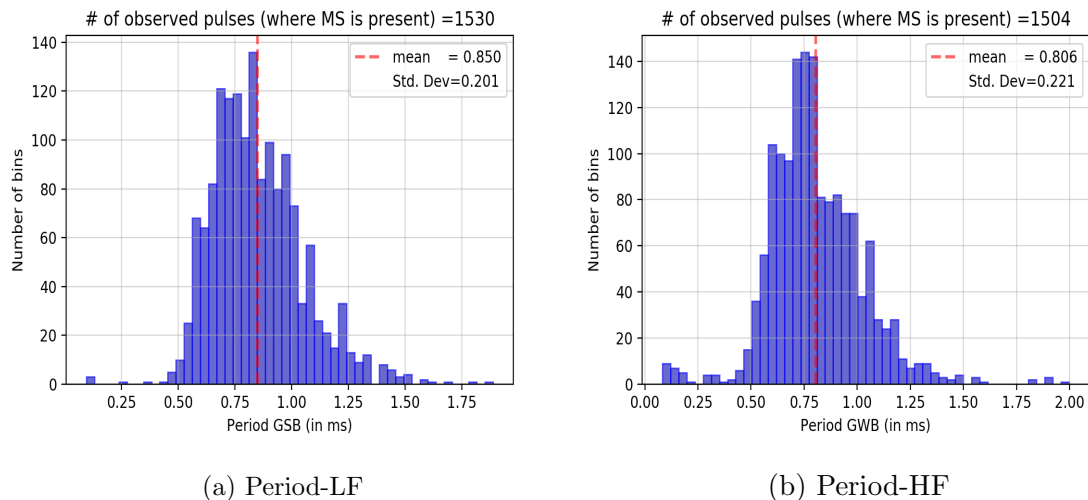


Figure 5-8: For pulsar B2016+28

5.3 FFT averaging

In the above graphs we observe that the value of the mean periodicities may not be properly detected due to a) Presence of noise in the signal, b) The choice of spurious peaks in the Fourier graph. To check the robustness of the histogram method, we have further developed a new method to visualise an average value of the periodicity of the pulsar.

In our analysis, we have seen that the quasi-periodicities are narrowly spread around a certain value. This implies that the spectrum of the individual pulses containing MS will always have a peak corresponding to the actual value of the period. This peak may sometimes be not detected (as the reasons stated above), but we can use this surity of being 'present' in a different way. We employ the technique of averaging the fourier of all the pulses where MS was found. This process take care of the spurios peaks which will be subdued in the process of averaging and only the 'constant' peak of the FFTs coming from the actual periodic MS will survive.

The average FFTs of the candidate pulsars were plotted along with the earlier plotted histograms, and the following properties were observed:

- The peak of the avg. FFT falls very close to the mode of the histograms.
- We can also see some secondary peaks which result from the harmonics of the microstructure signal. This not only shows that how well we are now able to see the spectrum (without noise), but also the fact that the smoothing preserves the features of Micro-structures.
- When the number of pulses (with MS) were observed, the histogram had a flat nature, and fails to give any result, however the folded FFT plot provides a reasonable estimate.

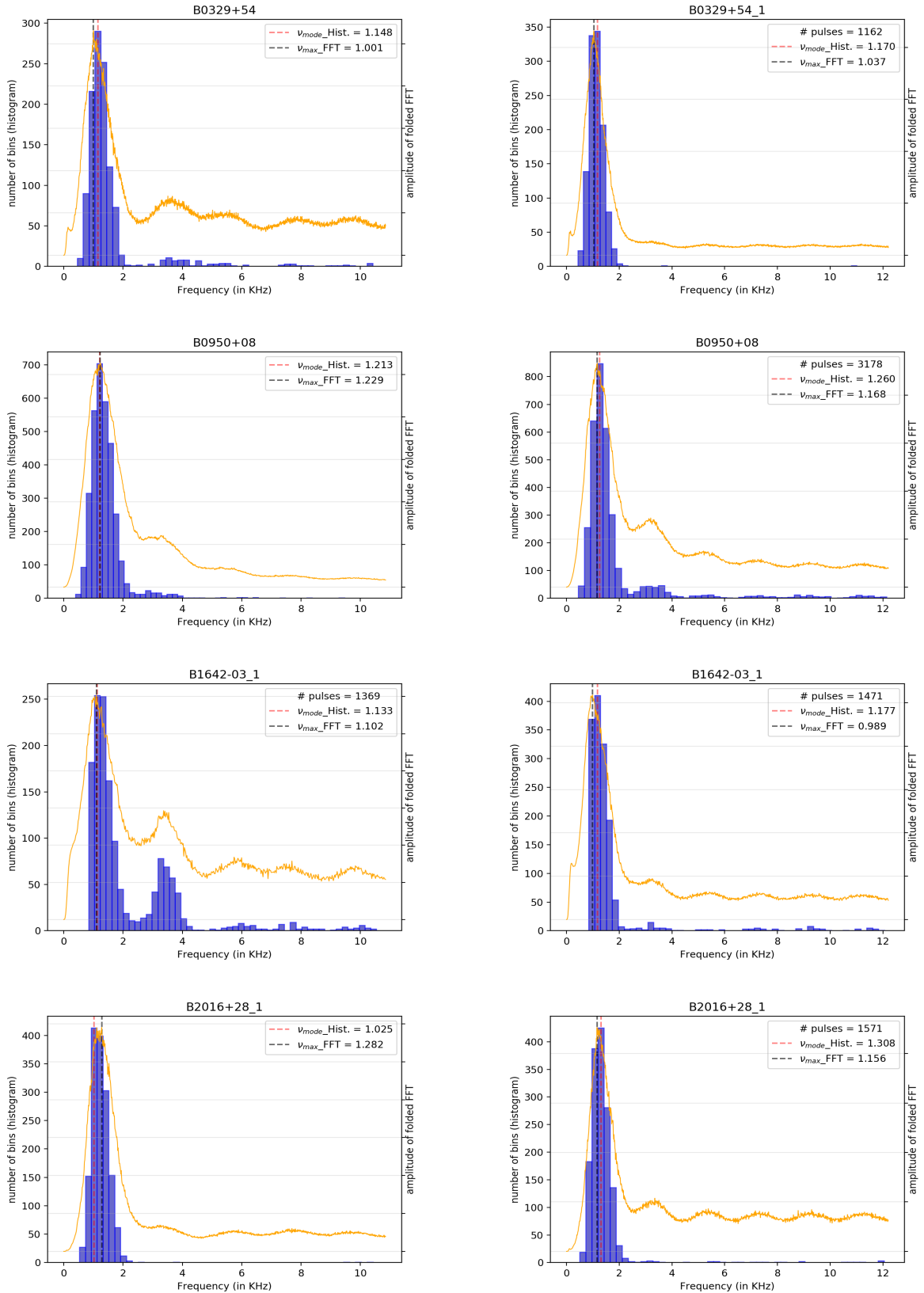


Figure 5-9: Folded FFT (in orange) compared with the histogram of the detected frequency. Left column is of the 310MHz, and the right one is of the 625MHz observation. Please note: that the frequency is shown in x-axis of the following graphs

5.4 Frequency evolution of microstructures

From section 3.4 (in figures 3-4 and 3-5), we observe that even after the alignment of the subpulses and folded profiles, there is a misalignment of the micropulse train as we move across the phases. A analysis was also proposed and is being implemented now. We know that the normalised cross-correlation function (CCF), after interpolation, gives a measure of similarity of two pulses wrt to the time-lag. We take the peak nearest to the 'zero-lag' as the reported delay of the micropulse trains between two frequencies. We choose different phase ranges of a given pulsar to see how the lag depends on the phase being selected. This is achieved by plotting the distribution of time-lag for a given phase range and seeing the mean of the histogram. The excecise was done in the B2016+28 and B0950+08 datasets.

5.4.1 CCF distribution in B2016+28 pulsar

The folded profile of the pulsar reveals that subpulses are concentrated in the region from 0.31 to 0.34 (fig. 3-3). Two distinct emission cones can be observed on either side of the phase with a saddle like structure in between. The phase range was divided into six different parts and the mean CCF lag was calculated for each of them.

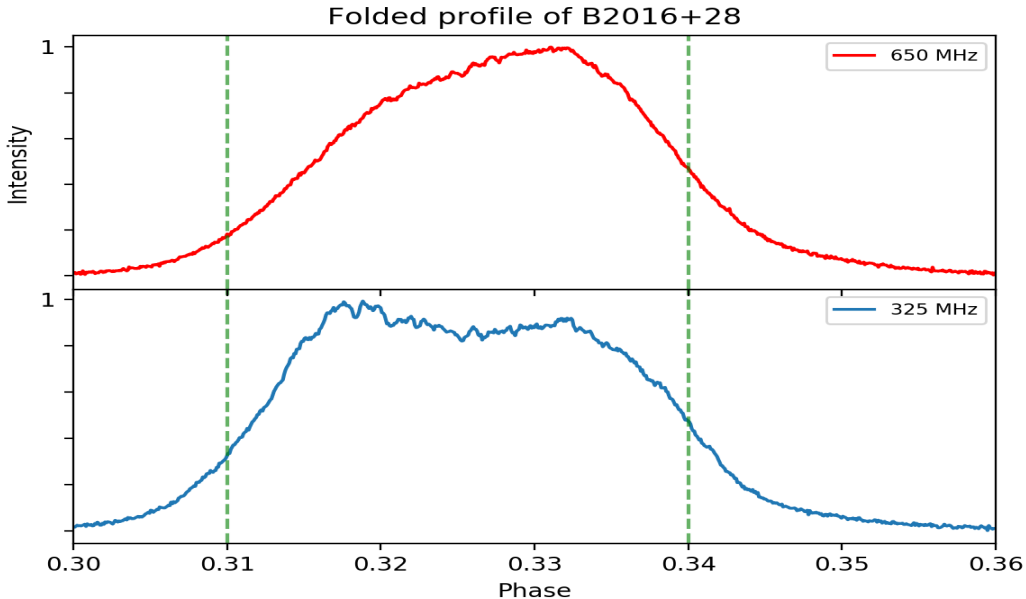
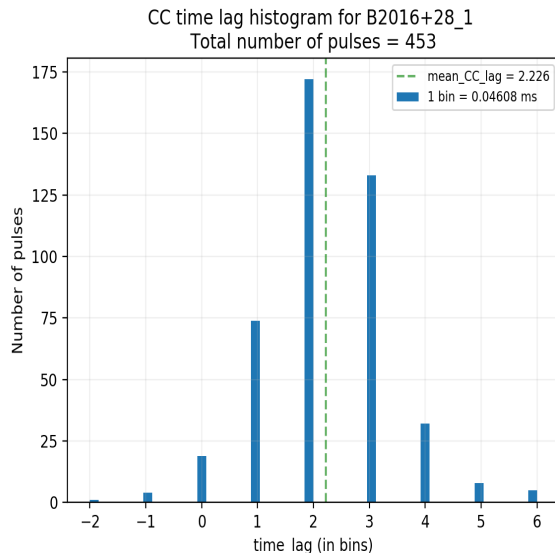


Figure 5-10: The folded profile of B2016+28 with the full range of chosen phase marked with green-dotted lines.

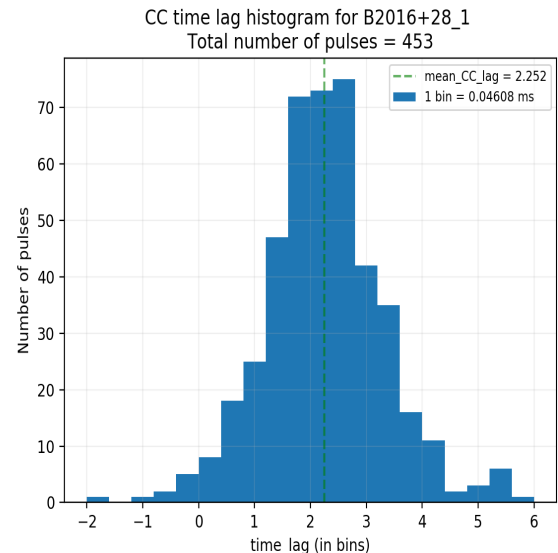
- Full window selected: (a) 0.310 to 0.314

- Further divided into six parts: (b) "0.310 to 0.315", (c) "0.315 to 0.320",
(d) "0.320 to 0.325", (e) "0.325 to 0.330", (f) "0.330 to 0.335", (g) "0.335 to 0.340"
- Total number of pulses with microstructures detected in (a): 453
- Total number of pulses with microstructures detected in (b): 7
- Total number of pulses with microstructures detected in (c): 100
- Total number of pulses with microstructures detected in (d): 170
- Total number of pulses with microstructures detected in (e): 180
- Total number of pulses with microstructures detected in (f): 131
- Total number of pulses with microstructures detected in (g): 52

For pulse window 0.31 to 0.34 (full)

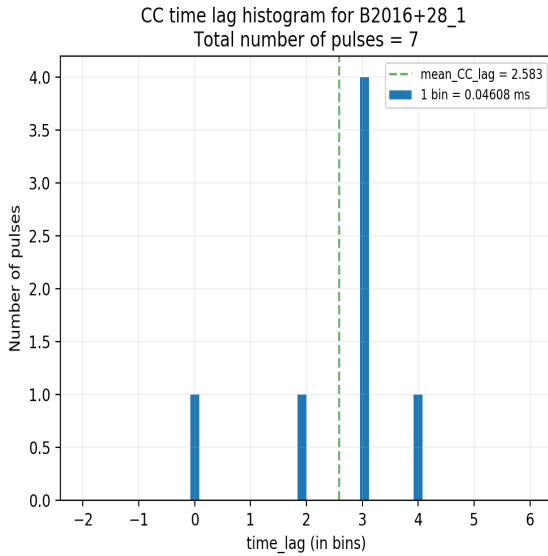


(i) Time lag from non- interpolated CCFs

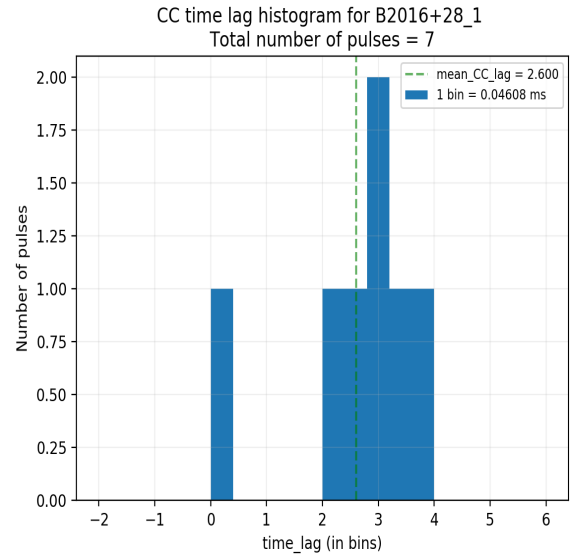


(ii) Time lag from Interpolated CCFs

For pulse window 0.310 to 0.315

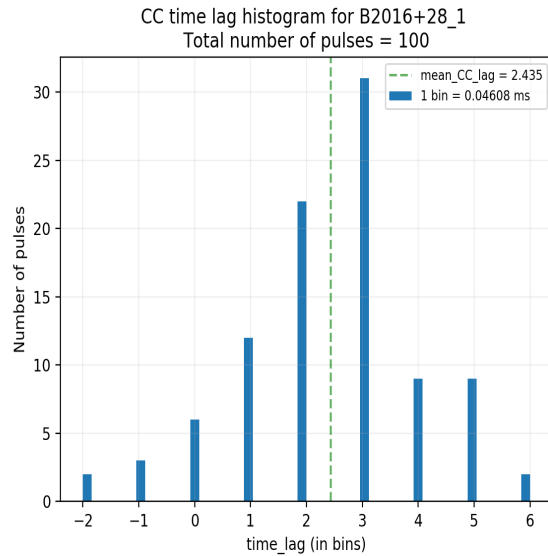


(i) Time lag from non- interpolated CCFs

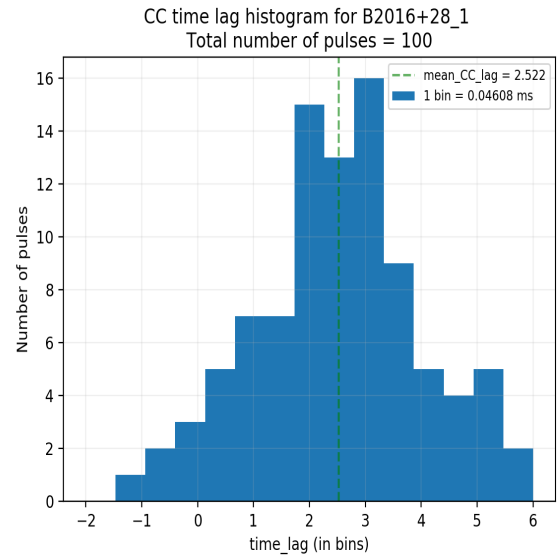


(ii) Time lag from Interpolated CCFs

For pulse window 0.315 to 0.320

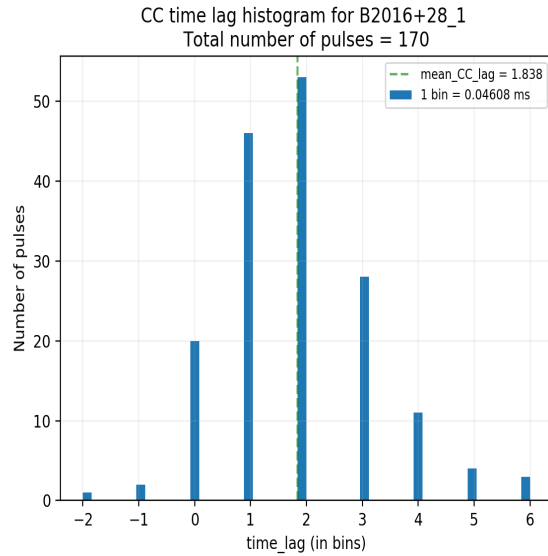


(i) Time lag from non- interpolated CCFs

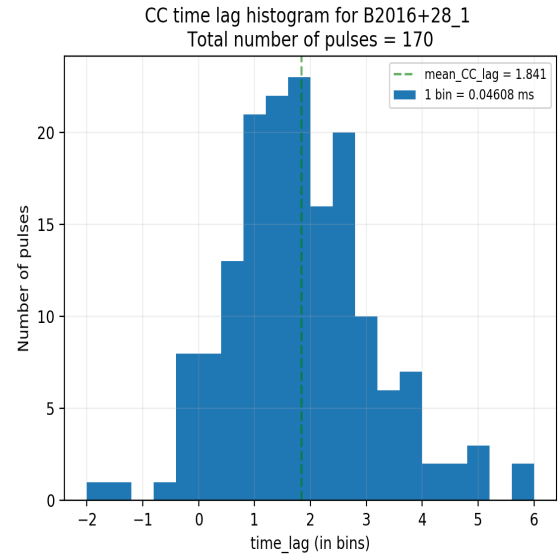


(ii) Time lag from Interpolated CCFs

For pulse window 0.320 to 0.325

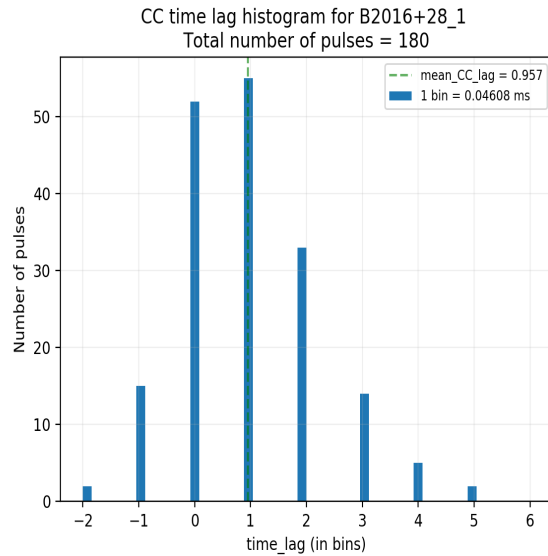


(i) Time lag from non- interpolated CCFs

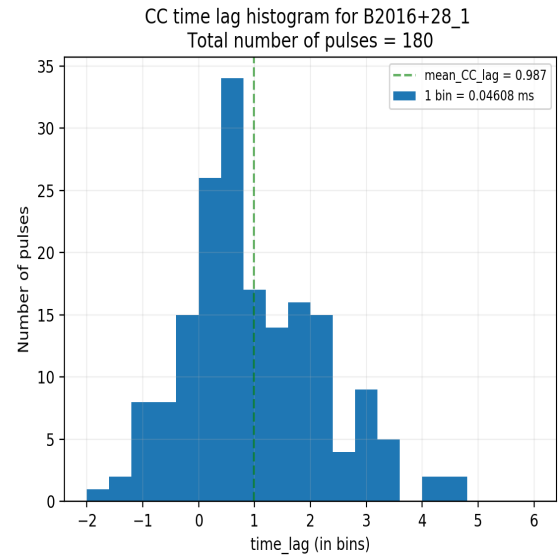


(ii) Time lag from Interpolated CCFs

For pulse window 0.325 to 0.330

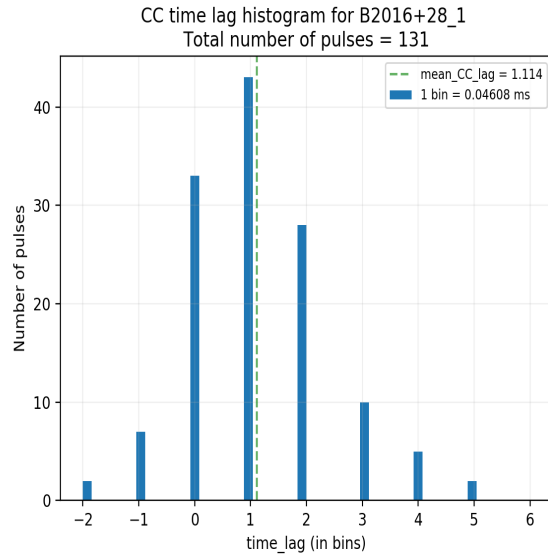


(i) Time lag from non- interpolated CCFs

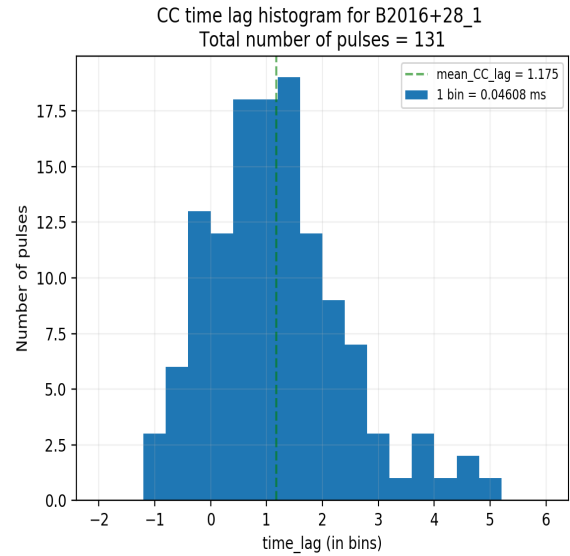


(ii) Time lag from Interpolated CCFs

For pulse window 0.330 to 0.335

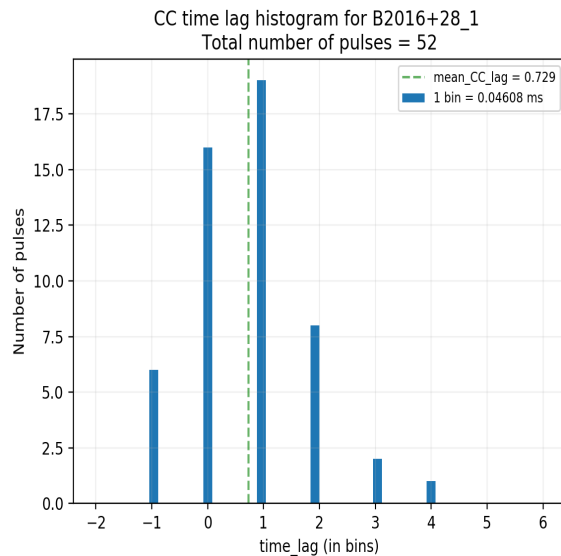


(i) Time lag from non- interpolated CCFs

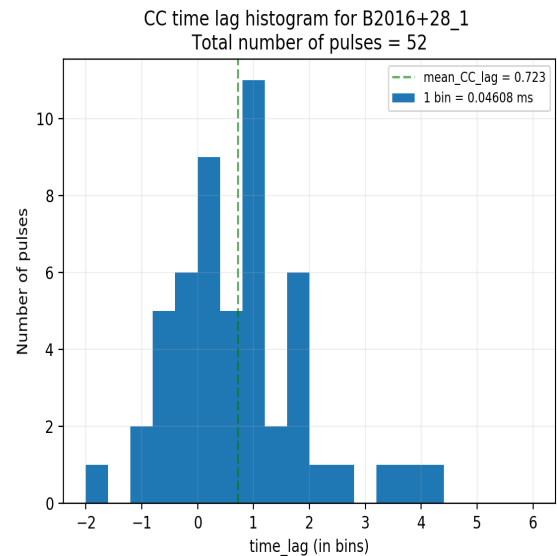


(ii) Time lag from Interpolated CCFs

For pulse window 0.335 to 0.340



(i) Time lag from non- interpolated CCFs



(ii) Time lag from Interpolated CCFs

5.4.2 CCF distribution in B0950+08 pulsar

The emission of the pulsar is constricted in the phase range of 0.74 to 0.82 (fig. 3-3). It was divided into six equal parts and the mean CCF lag was calculated for each of them. The pulsar was observed to have a significant number of simultaneous microstructure detection at both the frequency. Also, the intensity of the microstructure is comparatively much higher than the subpulse, hence we get a substantial number of pulses, even when we go for a smaller phase range. This gives us an opportunity to look into the pulses which are common to two or more phases implying that the micropulse train is present over multiple phases, and perform the analysis mentioned in section 4.7.3. Histograms of the time-lag for the CCFs(only interpolated) for the given phase are plotted. Mean time-lag (calculated from histogram) is mentioned in the respective graphs.

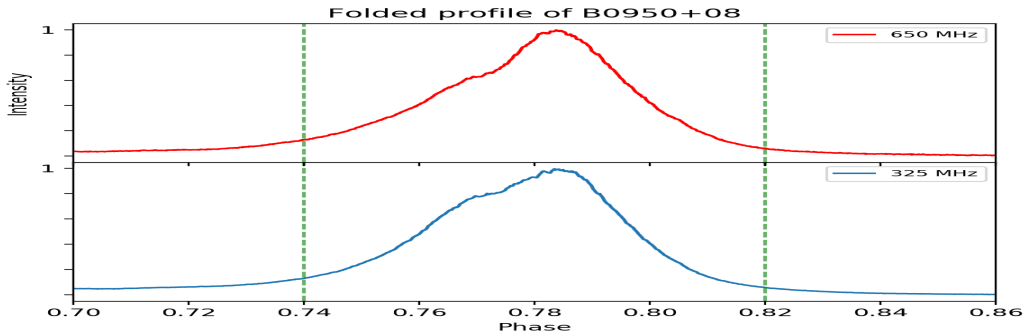
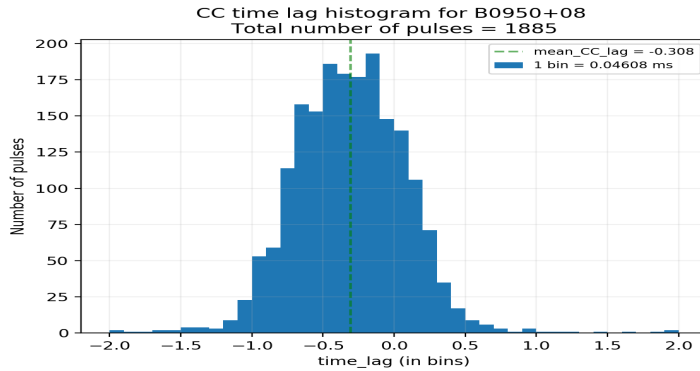


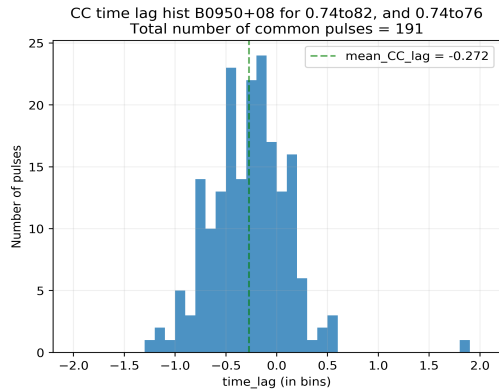
Figure 5-11: The folded profile of B0950+08 with the full range of chosen phase marked with green-dotted lines.

- Full window selected: **(a)** 0.74 to 0.82
- Further divided into four parts: **(b)** "0.74 to 0.76", **(c)** "0.76 to 0.78", **(d)** "0.78 to 0.80", **(e)** "0.80 to 0.82"
- Total number of pulses with microstructures detected in (a): 1885
- Total number of pulses with microstructures detected in (b): 193
- Total number of pulses with microstructures detected in (c): 1275
- Total number of pulses with microstructures detected in (d): 1622
- Total number of pulses with microstructures detected in (e): 321

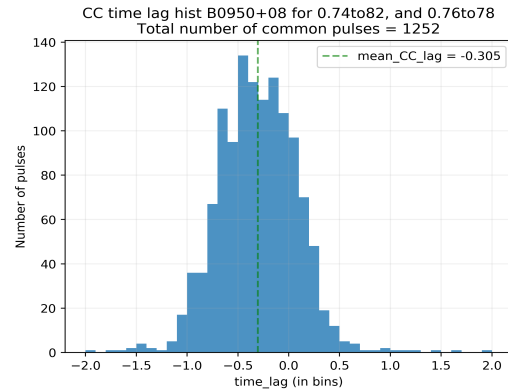
1. For pulse window 0.74 to 0.82 (full)



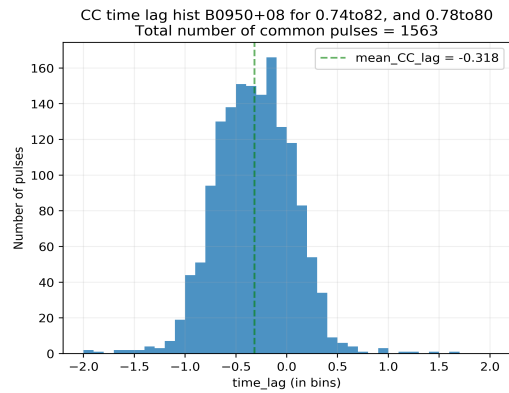
(i) For all the pulses detected in (a)



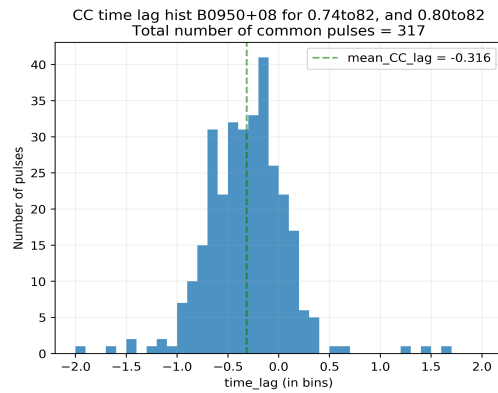
(ii) Common between (a) & (b)



(iii) Common between (a) & (c)

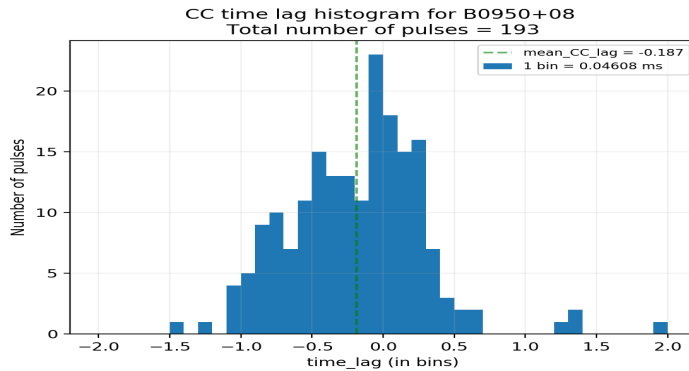


(iv) Common between (a) & (d)

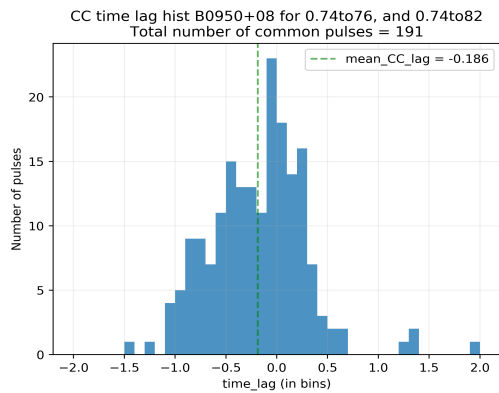


(v) Common between (a) & (e)

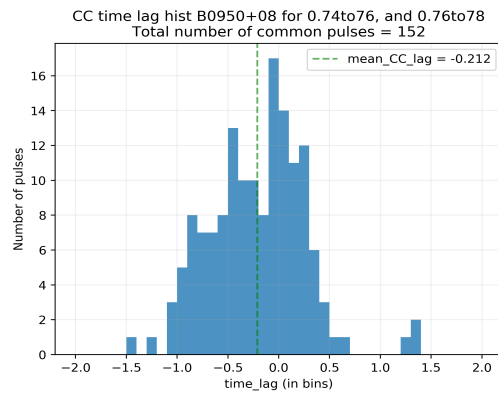
2. For pulse window 0.74 to 0.76:



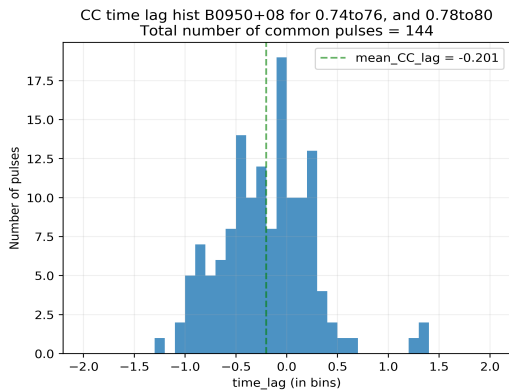
(i) For all the pulses detected in (b)



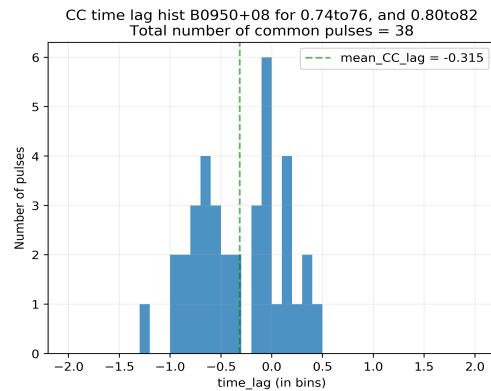
(ii) Common between (b) & (a)



(iii) Common between (b) & (c)

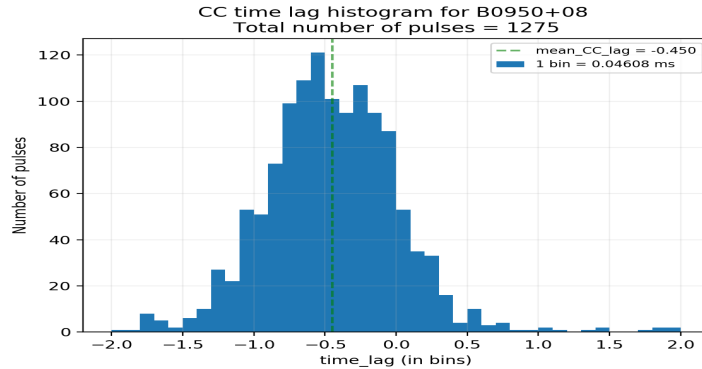


(iv) Common between (b) & (d)

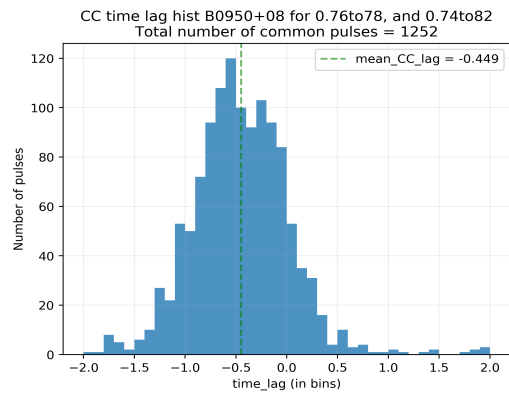


(v) Common between (b) & (e)

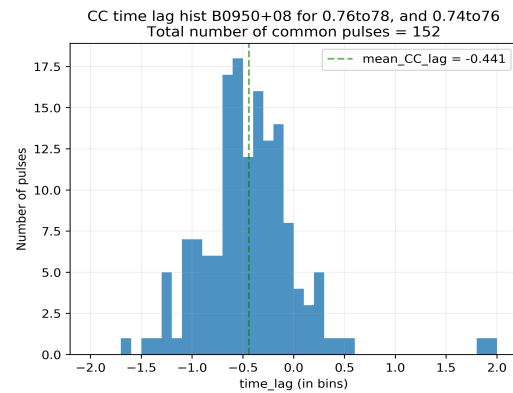
3. For pulse window 0.76 to 0.78:



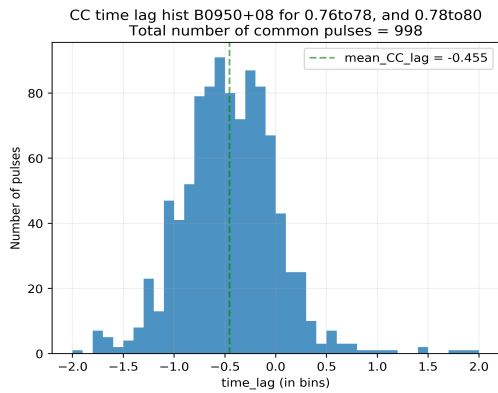
(i) For all the pulses detected in (c)



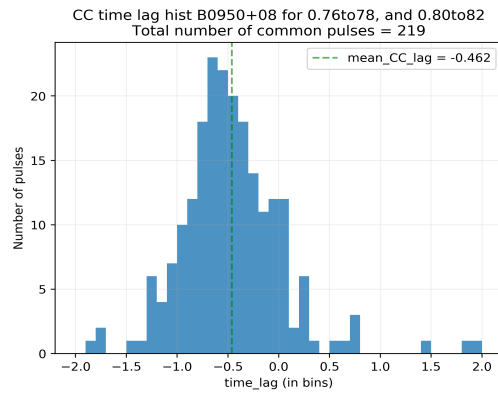
(ii) Common between (c) & (a)



(iii) Common between (c) & (b)

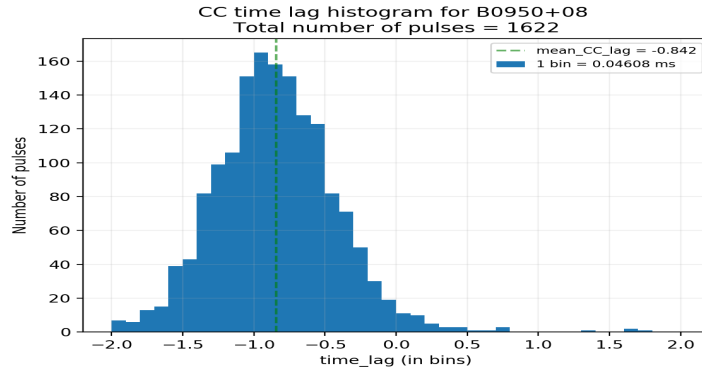


(iv) Common between (c) & (d)

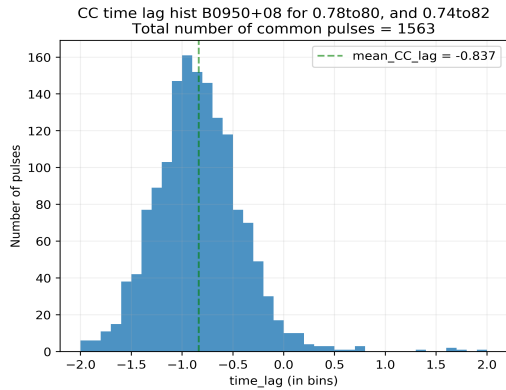


(v) Common between (c) & (e)

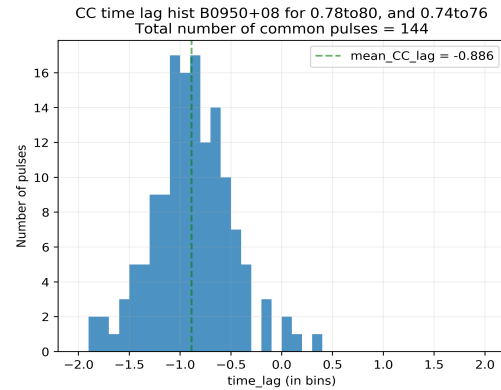
4. For pulse window 0.78 to 0.80:



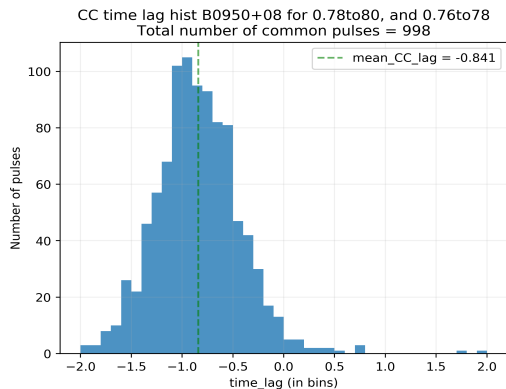
(i) For all the pulses detected in (d)



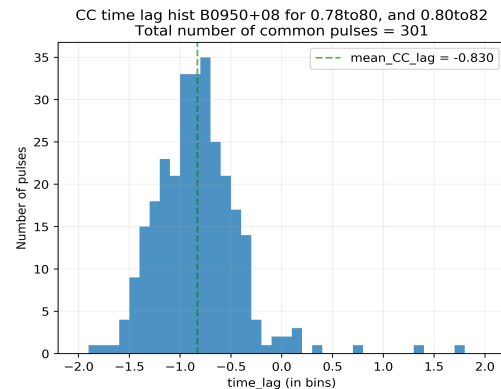
(ii) Common between (d) & (a)



(iii) Common between (d) & (b)

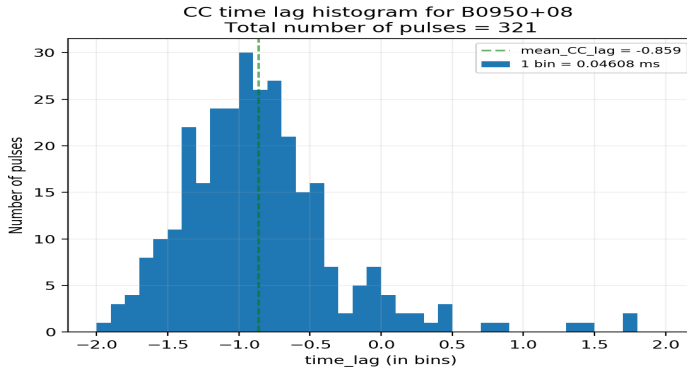


(iv) Common between (d) & (c)

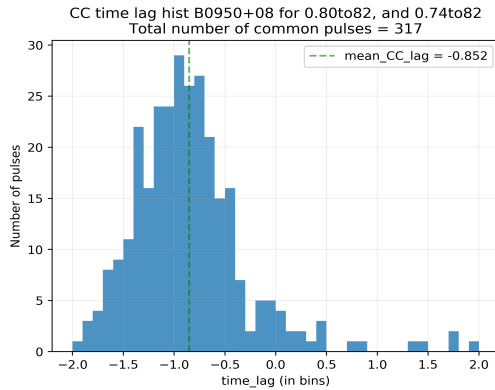


(v) Common between (d) & (e)

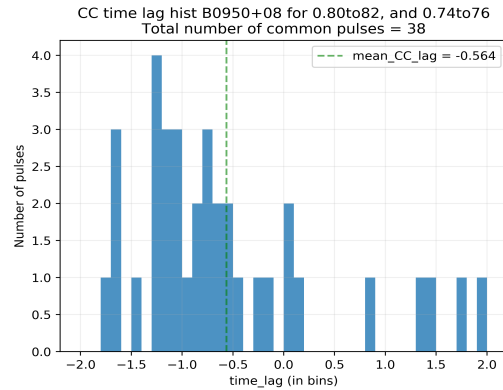
5. For pulse window 0.80 to 0.82:



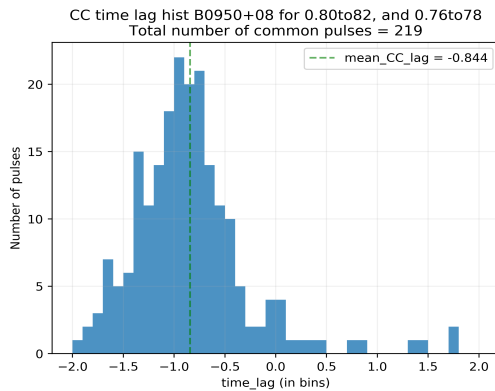
(i) For all the pulses detected in (e)



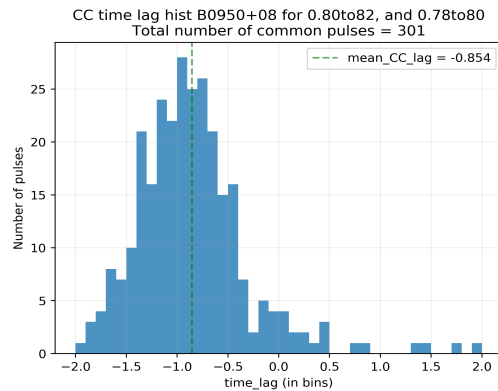
(ii) Common between (e) & (a)



(iii) Common between (e) & (b)



(iv) Common between (e) & (c)



(v) Common between (e) & (d)

Chapter 6

Discussion and Conclusion

In the previous chapters, we showed the observation method and data analysis process for microstructure quantification. Here we are interpreting our observed results.

6.1 Discussion

The microstructure of the investigated pulsars is found to be present in a varying fraction in pulsars at dual frequency. This result, combined with the fact that the structure is observed to appear over the whole frequency range where strong single pulses can be seen, supports the idea that microstructure is an important feature of pulsar radiation. It appears more likely that microstructure is closely connected to the emission process. In the following table, we summarise the values of width and the quasi-period of the microstructure observed on the two observational frequencies: 352 and 610 MHz.

6.1.1 Width distribution

		B0329+54	B0950+08	B1642-03	B2016+28
325 MHz	Mean	0.377	0.31	0.328	0.338
	Std. Dev	0.051	0.036	0.057	0.027
610 MHz	Mean	0.378	0.299	0.356	0.323
	Std. Dev	0.049	0.048	0.059	0.034

6.1.2 Periodicity distribution

From histogram

		B0329+54	B0950+08	B1642-03	B2016+28
325 MHz	Mean	0.818	0.800	0.634	0.850
	Std. Dev	0.276	0.243	0.285	0.201
610 MHz	Mean	0.936	0.742	0.785	0.806
	Std. Dev	0.239	0.290	0.230	0.221

From averaging the spectrum

		B0329+54	B0950+08	B1642-03	B2016+28
325 MHz	Mean	0.999	0.813	0.907	0.78
610 MHz	Mean	0.964	0.856	1.011	0.865

6.1.3 Frequency evolution of the microstructures and dependence on the phase range

The following tables contains the data from the graphs in the section 5.4. We have taken two pulsars for this case: B2016+28 (with total pulses = 2107) and B0950+08 (with total pulses = 5791). The "Pulses with MS" mentioned here are the ones where the microstructure was *detected on both the frequencies*. The time-lag reported is the mean of the distribution from the CCF plot for the given phase window.

a) For B2016+28

Phase	Pulses with MS	Non-interpolated CCF lag	Interpolated CCF lag
0.31 to 0.34 (full)	453	2.226	2.252
0.310 to 0.315	7	2.583	2.600
0.315 to 0.320	100	2.435	2.522
0.320 to 0.325	170	1.838	1.841
0.325 to 0.330	180	0.957	0.987
0.330 to 0.335	131	1.114	1.175
0.335 to 0.340	52	0.729	0.723

Table 6.1: Time-lag distribution with phase window in B2016+28

b) For B0950+08

Phase	Pulses with MS	Interpolated CCF lag
0.74 to 0.82 (full)	1885	-0.308
0.74 to 0.76	193	-0.187
0.76 to 0.78	1275	-0.450
0.78 to 0.80	1622	-0.842
0.80 to 0.82	321	-0.859

Table 6.2: Time-lag distribution with phase window in B0950+08

6.2 Conclusion

The high sensitivity of the upgraded GMRT, owing to its large bandwidths of operation, holds the potential to unravel microstructure emission in a much larger number of pulsars than currently possible. The results of the statistical analysis clearly show that a large number of pulses in our data set are detected with evidence of microstructure emission. The most important results that we have obtained are that:

1. MICROSTRUCTURE EMISSION: Our assumption that microstructures occur at of broadband is supported by the fraction of pulses with simultaneous microstructure

emission at both frequency. More number of microstructure pulses are detected in the intermediate phases due to more intensity of the signal in these windows.

2. WIDTH & PERIODICITY: They have statistically preferred widths and show quasiperiodicities. Same values of micropulse Widths and Periods at both frequency shows that microstructure characteristics are frequency independent. A better constraint of the MS periodicity was developed by using the average FFT method. The results obtained for B0329+54 are matching with previously reported study (Lange et al. 1998) at 4.85 GHz and (Kardashev et al. 1978) 102.5 MHz. Hence our analysis methods are working properly and better enough for micropulse quantification. Results for B2016+28 are same as reported (Mitra et al. 2015) at 1.1 GHz and (Cordes et al. 1990) at 430 MHz.
3. PROBING DUAL FREQUENCY NATURE: This type of study has been carried out for the first time. The data shows that there is a time-lag in microstructures between two observed frequencies. The alignment also depends upon the phase window being selected.
 - For B2016+28: The time-lag variation across the phases is significant. The value changes by almost two bins while going from the first window to the last one. From the folded profile, we note that there are two different emmission cones, the effect of it on the alignment is still to be probed.
 - For B0950+08: The microstructure train is mostly present significantly over a large phase window. This can be seen in the number of common pulses detected in two given phase window. There is a slight but a constant variation in the time-lag reported. The lag between the microstructure keeps on increasing as we move the phase window from "0.74-0.76" to "0.80-82".

6.3 Future work

We have seen how the microstructure evolve with the two observational frequencies. This offers us an opportunity to probe further into multiple frequency detection. The dependence of time-lag on the phase window is still to be performed to the other pulsars in the dataset.

Appendix A

Does smoothening by Savitzky-Golay preserve the microstructures' properties

The notion of a digital filter is most directly applicable to a series of *equally spaced data values* $f_i = f(t_i)$, where $t_i = t_0 + i\Delta$ for some constant sample spacing Δ and $i = \dots - 2, -1, 0, 1, 2\dots$. Then the simplest type of digital filter replaces each data value f_i by a linear combination g_i of itself and some number of nearby neighbours,

$$g_i = \sum_{n=-n_L}^{n_R} c_n f_{i+n} \quad (\text{A.1})$$

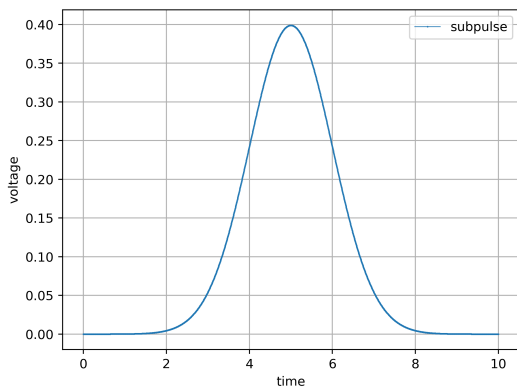
Here, n_L is the number of points used "to the left" of a data point i , i.e., earlier than it, while n_R is the number used to the right, i.e., later.

Rather than having their properties defined in the Fourier domain, and then translated to the time domain of the c_n 's, Savitzky-Golay filters derive directly from the time-domain problem of *data smoothing*.

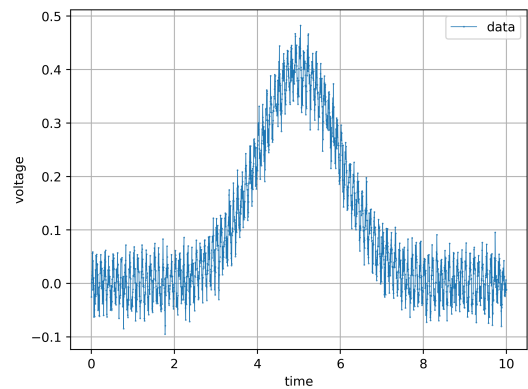
The premise of data smoothing is that one is measuring a variable that is both slowly varying and also corrupted by random noise. Then it can sometimes be useful to replace each data point by some kind of local average of surrounding data points. Since nearby points measure very nearly the same underlying value, averaging can reduce the level of noise without(much) biasing the value obtained.

As a starting point for understanding Savitzky-Golay filters, consider the simplest possible averaging procedure: for some fixed $n_L = n_R$, compute each g_i as the average of the data points from f_{i-n_L} to f_{i+n_R} . This is sometimes called moving window averaging and corresponds to equation(1) with constant $c_n = 1/(n_L + n_R + 1)$. If the underlying function is constant, or is changing linearly with time (increasing or decreasing),then no bias is introduced into the result. Higher points at one end of the averaging interval are on the average balanced by lower points at the other end. A bias is introduced, however, if the underlying function has a nonzero second derivative. At a local maximum, for example, moving window averaging always reduces the function value.

The idea of the Savitzky-Golay filtering is to find filter coefficients c_n that preserve higher moments. Equivalently, the idea is to approximate the underlying function within the moving window not by a constant (whose estimate is the average), but by a polynomial of higher order. For each point f_i , we least-squares fit a polynomial to all $n_L + n_R + 1$ points in the moving window, and then set g_i to be the value of that polynomial at position i . We make no use of the value of the polynomial at any other point. When we move on to the next point f_{i+1} , we do a whole new least-squares fit using a shifted window.

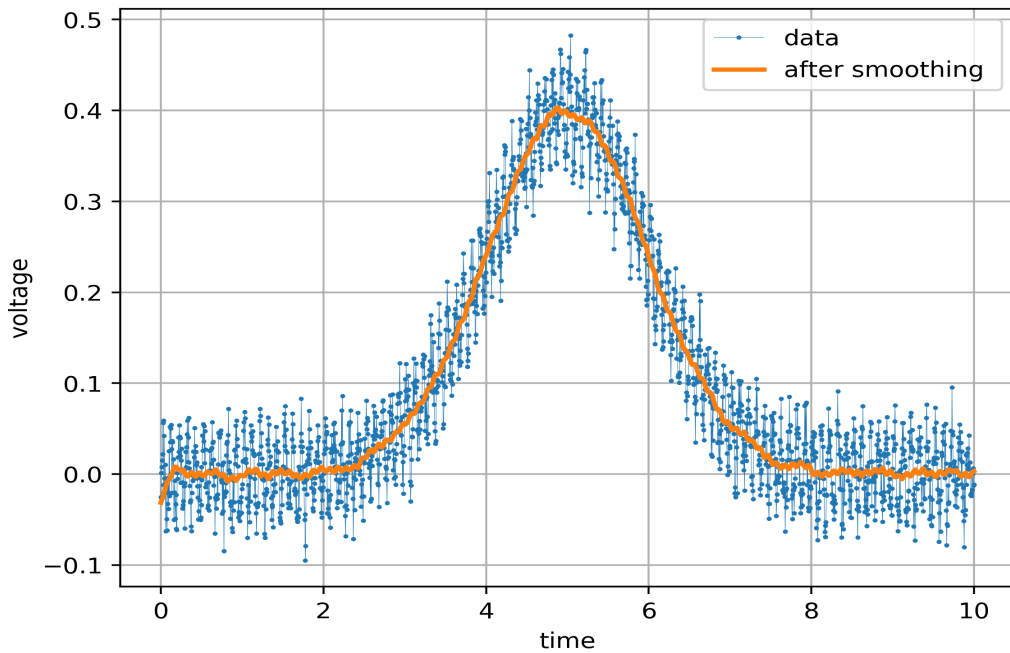


(a) Gaussian Signal with peak at 5

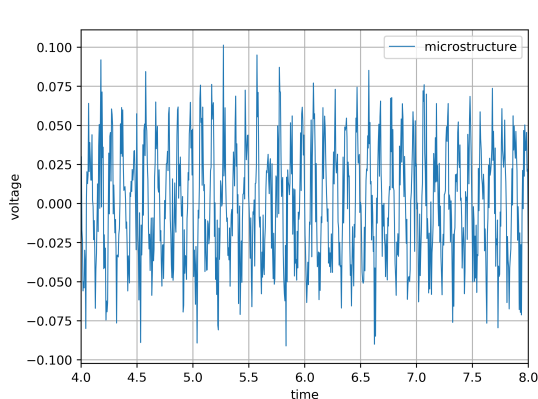


(b) Signal+Noise+MS

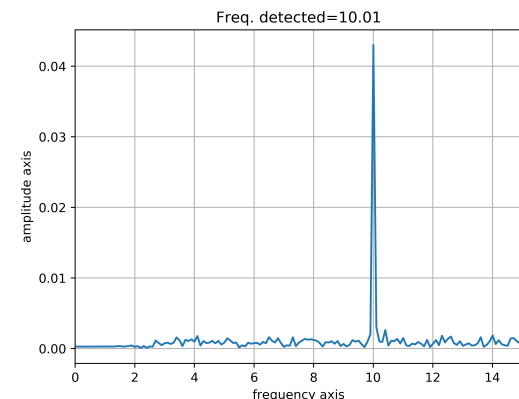
A Gaussian signal mixed with a random noise (with mean=0 and std. deviation = 0.02) and a simulated micro-structure with amplitude = 0.1 and frequency = 10. The resulting signal gets distorted but the periodicity can still be observed.



(a) Smoothing using SG-filter.



(a) Residual plot of MS+Noise



(b) Fourier of the residual plot

Thus we recover the mixed signal (MS+noise) without altering its property. FFT shows a peak at 10 which was the freq. of the added MS

To summarize: Within limits, Savitzky-Golay filtering does manage to provide smoothing without loss of resolution. It does this by assuming that relatively distant data points have a usable redundancy that can be used to reduce the level of noise.

Bibliography

- [1] Kishalay De, Yashwant Gupta, Prateek Sharma, 2016, *Detection of Polarized Quasi-periodic Microstructure Emission in Millisecond Pulsars*, Astrophysical Journal 833
- [2] Benford G., 1977, *Coherent pulsar radio radiation*, MNRAS 179, 311
- [3] Bhattacharya, D, 1998, NATO ASIC Proc. 515: The *Many Faces of Neutron Stars*.
- [4] Kishalay De and Yashwant Gupta, 2015, *A real-time coherent dedispersion pipeline for the giant metrewave radio telescope*, Experimental Astronomy, Volume 41 Number 1.
- [5] Gangadhara, R. T. & Gupta, Y., 2001, The Astrophysical Journal, Volume 555, Issue 1, pp. 31-39.
- [6] Hankins, T. H., Kern, J. S., Weatherall, J. C. & Eilek, J. A., 2003, *Nature*, Volume 422, Issue 6928, pp. 141-143.
- [7] J. M. Cordes, *The Astrophysical Journal*, 208:944-954, 1976 September 15.
- [8] J. M. Cordes, 1981, in Proc. of IAU Symposium nr.95: Pulsars, eds. R.Wielebinski, W. Sieber, pp 115
- [9] Kardashev, N.S., Kuzmin, A.D., Nikolaev, N.Ya., Novikov, A.Yu., Popov, M.V., Smirnova, T.V., Soglasnov, V.A., Shavanova, T.V., Shinskii, M.D., and Shitov, Yu.P.: 1978, Sov. Astron. 22 (5), pp. 583–587.
- [10] Lange, Ch., Kramer, M., Wielebinski, R. & Jessner, A., 1998, Astronomy and Astrophysics, v.332, p.111-120.
- [11] Lorimer, D. R. & Kramer, M., 2004, *Handbook of pulsar astronomy*. Cambridge observing handbooks for research astronomers, Vol. 4. Cambridge, UK: Cambridge University Press.
- [12] Mitra, D.; Arjunwadkar, M., Rankin, J. M., 2015, The Astrophysical Journal, Volume 806, Issue 2, article id. 236, 25 pp